Influence of synthetic inlet turbulence on the prediction of low Mach number flows

João Marcelo Vedovoto, Aristeu da Silveira Neto, Luis Fernando Figueira da Silva, Arnaud Mura

Influence of synthetic inlet turbulence on the prediction of low Mach number flows

João Marcelo Vedovoto

Faculty of Mechanical Engineering, Federal University of Uberlândia, Uberlândia-MG, 38400-902 Brazil

Corresponding author: Prof. João Marcelo Vedovoto, Dr. Ing., jmvedovoto@mecanica.ufu.br, phone: +55 34 32 39 40 40, fax: +55 34 32 39 41 42

Aristeu da Silveira Neto

Faculty of Mechanical Engineering, Federal University of Uberlândia, Uberlândia-MG, 38400-902 Brazil

Luis Fernando Figueira da Silva

Pontifícia Universidade Católica do Rio de Janeiro - Department of Mechanical Engineering - Rio de Janeiro-RJ, 22453-900 Brazil

Arnaud Mura

Institut Pprime, UPR3346 CNRS - ENSMA and University of Poitiers - BP40109 - 86961, Poitiers, France

---

Abstract

Time-resolved numerical simulations of fluid flows, such as Large Eddy Simulations (LES), have the capability of simulating the unsteady dynamics of large scale energetic structures. However, they are known to be intrinsically sensitive to inflow conditions the modelling of which may become a crucial ingredient of the computational model. The present work reports LES of both reactive and non-reactive turbulent channel flows. The flow configuration and associated conditions correspond to those associated with a reference experimental database that has been gathered at the French aerospace Laboratory of Onera. The focus of our study is placed on the influence of synthetic inlet turbulence in this experimental geometry, i.e., the principal aim is to investigate the sensitivity of the flow dynamics and mixing to inflow conditions. The analysis undoubtedly confirms that, even with properly set mean velocity and turbulence kinetic en-

ergy profiles as available from experimental data, both non-reactive and reactive flow fields still remain very sensitive to the choice of the synthetic turbulence model. This sensitivity is illustrated for four distinct turbulent inflows obtained from *white noise* (WN), *digital filter* (DF) by Klein et al. (2003), *random flow generator* (RFG) by Smirnov et al. (2001), and *synthetic eddy model* (SEM) by Jarrin et al. (2009). Finally the results obtained for reactive flow conditions clearly emphasize the influence of the retained model on the chemical reaction rate statistics. This conclusion confirms how relevant are the developments devoted to synthetic turbulence for the computational investigation of turbulent combustion.

Keywords: Turbulent inflow boundary conditions, Large Eddy Simulation, Synthetic inlet turbulence, Low Mach number flows, Reactive flows

1. Introduction

It is well known that a subject of great importance for fluid flow numerical simulations is the prescription of correct and realistic boundary conditions. For outflow conditions, it appears that the use of a buffer zone (Bodony, 2006) or an advective boundary condition (Orlanski, 1976), or even a combination of both, may adequately describe several flow conditions of practical interest. The present work is focused on low Mach number flows and the main difficulty is thus concentrated on the settlement of the inlet velocity field. In contrast, for compressible flows, specifying the fourth variable (pressure, density, temperature or characteristic wave) may also become a critical issue which raises a wide range of additional specific difficulties. In such conditions, elaborate strategies should be used to avoid pressure wave reflections, see for instance Rudy and Strikwerda (1980); Thompson (1987); Poinsot and Lele (1992); Albin et al. (2011). The specification of inflow boundary conditions may also raise several issues. Most flows encountered in real applications are, indeed, spatially developing turbulent flows. Hence, they pose a great challenge for numerical simulations due to the

need to prescribe time-dependent turbulent inflow data at the upstream boundary. For steady Reynolds-Averaged Navier-Stokes (RANS) simulations, simple analytical or experimental profiles are retained for mean velocity components and turbulent characteristics. For LES or Direct Numerical Simulations (DNS), however, the inflow data should consist of an unsteady fluctuating velocity signal representative of the turbulent velocity field at the inlet.

A basic technique to generate such a turbulent inflow data consists in taking a mean velocity profile with superimposed random noise. The major drawback of such a methodology is that the resulting inflow data do not exhibit any spatial and/or temporal correlations. The energy generated is, also, uniformly spread over all wave numbers and, due to the lack of large scale energy-containing structures, *turbulence* is quickly dissipated (Jarrin et al., 2009).

In principle it may be possible to predict turbulence via a LES technique by starting from a quiescent flow or with the mean flow field obtained from RANS simulations. Unfortunately, a very long time is required for a turbulent flow to spatially and temporally develop (Smirnov et al., 2001). Ideally, the simulation of the upstream flow entering a computational domain would provide realistic inlet conditions to the simulation of interest. However, due to the computational cost, the domain cannot be extended upstream indefinitely, and approximate turbulent inlet conditions must therefore be specified.

There are several ways to remedy this situation, and the existing methods belong to two principal categories: *(i) mapping or recycling methods*, in which some sort of turbulent flow is pre-computed, prior to the main calculation, and subsequently introduced at the domain inlet, and *(ii) synthetic turbulence methods*, in which some form of random fluctuation is generated, modulated according to experimental data, and combined with mean inflow. Other appealing strategies have been introduced in the literature, some of them are based on Fourier techniques, and others rely on the Proper Orthogonal Decomposition (POD) introduced by Lumley (1967), see for instance Druault et al. (2004).

The present manuscript is organized as follows: first a brief description of recycling methods is provided. Further, synthetic turbulence generators are pre-

sented, and the four methods considered in the present work are detailed: (i) the *white noise* (WN), (ii) the digital filter (DF) method proposed by Klein et al. (2003), (iii) the *Random Flow Generator* (RFG) introduced by Smirnov et al. (2001) and (iv) the *Synthetic Eddy Method* (SEM) of Jarrin et al. (2009). The synthetic turbulence generators have been implemented in a low Mach number Navier-Stokes solver, the main features of which are presented, including a brief description of both mathematical and numerical aspects. As a preliminary step of verification and validation, the methods are applied to the description of homogeneous isotropic turbulence. The computational programs are then further assessed by analyzing their capabilities of generating a fluctuating signal which reproduces a given stress tensor and features an energy spectrum similar to the one associated with a fully developed turbulent flow spectrum. The former means that the inflow data generator should be able to reproduce an anisotropic turbulent velocity field at the inlet. The paper ends with the application of the above-mentioned synthetic turbulence generators to the numerical simulation of high speed non-reactive and reactive turbulent mixing layers, which were experimentally studied by Moreau and Boutier (1977), see also Magre et al. (1988). Comparisons with available experimental data are provided.

2. Literature review

The specification of realistic turbulent inflow boundary conditions remains a challenging issue for both LES and DNS. This is quite a contrast to RANS or URANS applications for which a scale separation argument is implied between the unsteadiness of the mean flow field and the associated turbulent fluctuations. The quantities being computed in RANS or URANS are thus steady or varying on a characteristic time scale that is much larger than the computational time step. Such a scale separation argument does not hold for DNS or LES which therefore require a special treatment of turbulent fluctuations at inlet conditions. A review of some of the existent methods that deal with the specification of such turbulent inflow conditions is provided below.

2.1. Mapping methods

The most accurate method to specify turbulent fluctuations for either LES or DNS would probably consist in running a suitable precursor simulation with the purpose of providing the main simulation with accurate boundary conditions. However, such a procedure has been used only when the turbulence at the inlet can be regarded as a fully developed or a spatially developing boundary layer. In these cases periodic boundary conditions in the mean flow direction can be applied to the precursor simulation. In general, the simulation of the precursor flow is initialized with a mean velocity profile perturbed with a few unstable Fourier modes. Instantaneous velocity fluctuations in a plane positioned at a fixed streamwise location are extracted from the precursor simulation and prescribed at the inlet of the main simulation at each time step.

In practice, periodic boundary conditions can only be used to generate inflow conditions for homogeneous flows in the streamwise direction, which restricts their applications to simple fully developed flows. A more flexible technique to generate inlet conditions, also based on the procedure of recycling the velocities in a plane located several boundary layer thicknesses downstream of the inlet, has been proposed by Lund (1998). In this framework, the velocity field at the re-scaling station is decomposed into mean and fluctuating components; scaling is applied to the mean and to the fluctuating parts in the inner and outer layers to account for the different similarity laws that govern both regions. The scaled velocity is then re-introduced as a boundary condition at the inlet of the computational domain. The use of such a methodology results in a spatially evolving boundary layer simulation that is capable of generating its own inflow data.

Another strategy has been followed by Li et al. (2000) who proposed a procedure to reduce the storage requirement, as well as the computational cost associated with a precursor calculation. A spatially developing turbulent mixing layer, originating from the mixing of a low-speed and a high-speed boundary layer flow at the end of a splitter plate, is simulated within the LES context. However, instead of simulating the precursor boundary layer flow fields, only a

time series of instantaneous velocity planes with duration approximately equal to the integral time scale of the flow is extracted from a boundary layer simulation. The resulting signal is converted into a periodic one using a classic windowing technique, and it is used, as many times as required, to obtain converged statistics in the main simulation. This methodology is beneficial from both the computational and storage points of view, since the precursor simulation is run over a short duration only and the data used to generate the inflow correspond to a few integral time scales of the flow. For the investigated mixing layer simulation, the periodicity involved by the inflow decays rapidly, in approximately 25 per cent of the total length of the computational domain. However, Li et al. (2000) reported that the resort to this procedure for wall-bounded flows, where destabilizing effects remain relatively weak, might require a longer transition region to weaken the effects of the periodicity condition that is involved in the inflow prescription.

Finally, Bodony (2006) noted that the method introduced by Lund (1998), i.e., random uncorrelated fluctuations superimposed on a mean velocity profile, is very sensitive to the initialization of the flow field. Bodony (2006) also stated that the generation of fully developed turbulence cannot be obtained from such a strategy and, hence, proposed a more robust variant of the original method of Lund (1998), where the flow field is initialized thanks to synthetic turbulence with prescribed energy spectrum and shear stress profile.

To conclude it is noteworthy that other mapping techniques have been proposed in the context of hybrid RANS-LES simulations. For instance, Schlüter et al. (2004) fed the LES of a combustor with the Favre-averaged mean velocity field $\widetilde{u}_i$ issued from a RANS solution together with a fluctuating component $u_i - \widetilde{u}_i$. The latter is extracted from a database which was generated from an auxialliary LES computation and the corresponding turbulent fluctuations are rescaled to match mean and fluctuations statistics issued from the RANS simulation.

2.2. Synthetic turbulence generators

Methods that do not rely on a precursor simulation, or re-scaling of a database obtained from a precursor simulation, synthesize inflow conditions using some sort of stochastic procedure. These procedures use random number generators to build a fluctuating velocity signal similar to those observed in turbulent flows. This is possible based on the assumption that a turbulent flow can be approximated from a set of low order statistics, such as mean velocity, turbulent kinetic energy, Reynolds stresses, two-point or two-time correlations. However, it is worth emphasizing that the resulting synthesized signals remain only a crude approximation of turbulence. From a statistical point of view, some crucial quantities, such as the dissipation rate, the turbulent transport or the pressure-strain term that appear in the Reynolds stresses balance are often not well reproduced. The dynamics of the turbulent eddies are not perfectly recovered, and the synthesized flow may undergo a transition to turbulence. Therefore, synthesized turbulence can have a structure that significantly differs from that of the real flow fields (Jarrin et al., 2009).

2.2.1. White noise based synthetic turbulence generators - WN

The most straightforward approach to build synthetic fluctuations is to generate a set of independent random numbers between zero and unity which can *mimic* the turbulence intensity at the inlet. Indeed, if the turbulent kinetic energy level k is known, it can be used to scale a random signal $\mathcal{R}_{u_i}$ with zero mean and unity variance. Thus, the fluctuations exhibit the correct level of turbulent kinetic energy, which yields $u_i = \widetilde{u}_i + \mathcal{R}_{u_i}\sqrt{2k/3}$, where $\mathcal{R}_{u_i}$ is taken from independent random variables for each velocity component at each instant and location on the computational inlet plane. This procedure generates an isotropic random signal that reproduces both the mean velocity and turbulent kinetic energy levels. However, the signal generated does not present any two-point nor two-time correlations.

If the Reynolds stresses tensor (R_{ij}) is available, Lund (1998) introduced the

following transformation rule to reconstruct correlated velocity components:

$$u_i = \widetilde{u}_i + \mathcal{R}_{u_j} a_{ij}, \tag{1}$$

where (a_{ij}) denotes the Cholesky decomposition of the symmetric positive defined Reynolds stress tensor (R_{ij}),

$$a_{ij} = \begin{pmatrix} \sqrt{R_{11}} & 0 & 0 \\ R_{21}/a_{11} & \sqrt{R_{22} - a_{21}^2} & 0 \\ R_{31}/a_{11} & (R_{32} - a_{21}a_{31})/a_{22} & \sqrt{R_{33} - a_{31}^2 - a_{32}^2} \end{pmatrix}. \tag{2}$$

This strategy allows the basic random procedure to reproduce the targeted cross-correlations between velocity components.

Although the methods presented above are capable of reproducing some characteristics of real turbulent flow fields, such as the anisotropy, they do not account for any correlations in either time or space. Therefore, these random fluctuations have their energy sprectrum uniformly spread over all wave numbers and, as already stated above, this energy will be quickly dissipated downstream of the inlet boundary. A more valuable approach for generating synthetic turbulence therefore consists in creating bins of random data, which can then be processed using digital filters, so that the resulting set of processed data will display desired statistical properties, such as spatial and temporal correlations (Lund, 1998; Klein et al., 2003).

2.2.2. Digital filters based synthetic turbulence generators - DF

Klein et al. (2003) proposed a digital filtering (DF) procedure to remedy the lack of large-scale correlation in the inflow data generated through the above method. In one dimension the fluctuating velocity signal u'_m at a point m is defined as a convolution or a digital linear non-recursive filtering:

$$u'_m = \sum_{n=-M}^{n=M} b_n \mathcal{R}_{m+n}, \tag{3}$$

where $\mathcal{R}_m$ is a series of random data generated at point m with $\overline{\mathcal{R}}_m = 0$, $\overline{\mathcal{R}_m \mathcal{R}_m} = 1$, $\overline{\mathcal{R}_m \mathcal{R}_n} = 0$ for $m \neq n$, and b_n are the filter coefficients. In the

previous expressions, the overbar denotes averaged values obtained from the series of random data. Note that, since the ergodic hypothesis is implied, the time average of one sequence of events is the same as the ensemble average. The integer number M is related to the size of the filter support. The relation between the filter coefficients and the two-point velocity correlation function is given by:

$$\frac{\sum_{j=-M+k}^{j=M} b_j b_{j-k}}{\sum_{j=-M}^{j=M} b_j^2} = \frac{\overline{u'_m u'_{m+k}}}{\overline{u'_m u'_m}} \tag{4}$$

This procedure is extended to the time-dependent generation of synthetic velocity field on a plane (Ox_2x_3) by generating a three-dimensional random field $\mathcal{R}_m(i,j,k)$ for each velocity component m. The indices i, j, and k are associated to the x_1-direction (or time t by making use of the Taylor hypothesis), the x_2-direction and the x_3-direction, respectively. A three-dimensional filter $b(i,j,k)$ is obtained by the convolution of three one-dimensional filters: $b(i,j,k) = b_i \times \times b_j \times b_k$, in such a manner that the random data $\mathcal{R}_m(i,j,k)$ are filtered in the three directions x_1, x_2 and x_3,

$$\mathcal{U}_m(j,k) = \sum_{i'=-M_{x_1}}^{i'=M_{x_1}} \sum_{j'=-M_{x_2}}^{j'=M_{x_2}} \sum_{k'=-M_{x_3}}^{k'=M_{x_3}} b_{i'} \times b_{j'} \times b_{k'}\ \mathcal{R}_m(i', j+j', k+k') \tag{5}$$

where j and k denote the location of the computational cell at the inlet plane, i.e., $j = 1, ..., N_{x_2}$ and $k = 1, ..., N_{x_3}$. Note that, in the following, we will retain an homogeneous filter width N in the three spatial directions, i.e., M_{x_1}=M_{x_2}=M_{x_3}=N.

In order to generate fluctuations that reproduce exactly the targeted two-point correlations, the filter coefficients b_k should be computed by inverting Eq. (4). However, since the two-point autocorrelation tensor is seldom available, Klein et al. (2003) assumed a Gaussian shape depending on one single parameter, the length scale $L = n\Delta x$ (N being such that $N \geq 2n$). The coefficients can then be computed analytically, without the cost of inverting Eq. (4), $b_p \approx$

$\hat{b}_p / \sqrt{\left(\sum_{j=-N}^{j=N} \hat{b}_j^2\right)}$ where $\hat{b}_j := \exp\left(-\pi j^2/2n^2\right)$. Once the processed random signal is evaluated by using Eq. (5), the final inflow velocity can be written as, $u_i = \widetilde{u}_i + a_{im}\mathcal{U}_m(j,k)$ thanks to the Cholesky decomposition a_{ij} of the Reynolds stress tensor R_{ij}.

Following Klein et al. (2003), it is possible to generate a large amount of data, store and convect it through the inflow plane by applying Taylor's hypothesis. However, for the applications considered here, the inflow data will be generated on-the-fly. The implementation of the DF synthetic turbulence generator is indeed quite efficient and, for the present application, the computational costs associated to the database lookup technique were found greater than the online generation of the data. We therefore preferred to resort to the latter.

It should be noted that the main parameters retained to evaluate this method are the choice of the length scales, which are directly connected to the DF support size, and the dimensions of the control volume. Thus, a given value of the characteristic length scale may be reproduced by correctly choosing the filter support size as well as the control volumes dimensions. However, as will be shown below, the length scales and, consequently, the filter support size strongly impact on the computational cost of the method. Finally, since a fixed computational grid is used here to assess the different turbulent inflow generators, the parameters retained to evaluate the DF method will be the support size, only.

2.2.3. Synthetic turbulence generators based on Fourier techniques - RFG

In their recent review, Tabor and Baba-Ahmadi (2010) concluded that, since turbulence is often analyzed on the basis of a harmonic functions decomposition, i.e., Fourier analysis, the fluctuations can be more efficiently represented by resorting to a linear sum of trigonometric functions, with the coefficients representing the energy contained in each mode.

To the authors best knowledge, Kraichnan (1970) was the first to use a Fourier decomposition to generate a synthetic fluctuating turbulent flow field. In Kraichnan's early work, the flow is initialized with a three-dimensional homo-

geneous and isotropic synthetic velocity field to study the diffusion of a passive scalar. Since the velocity fluctuations are homogeneous in the three dimensions, they can be decomposed in the Fourier space, $\mathbf{u}'(\mathbf{x}) = \sum_{\mathbf{k}} \hat{\mathbf{u}}'_{\mathbf{k}} e^{-i\mathbf{k}.\mathbf{x}}$, where $\mathbf{k}$ is a three-dimensional wave number vector. Each complex Fourier coefficient $\hat{\mathbf{u}}'_{\mathbf{k}}$ defines an amplitude evaluated from a prescribed isotropic three-dimensional energy spectrum $E(|\mathbf{k}|)$ and a random phase $\theta_{\mathbf{k}}$, taken uniformly in the $[0, 2\pi]$ interval (Rogallo, 1981). The synthesized velocity field is thus given by $\mathbf{u}'(\mathbf{x}) = \sum_{\mathbf{k}} \sqrt{E(|\mathbf{k}|)} e^{-i(\mathbf{k}.\mathbf{x}+\theta_{\mathbf{k}})}$. Several adaptations of Kraichnan's method were proposed throughout the years. Among them, Lee et al. (1992) proposed one that allows for the application of Kraichnan's method to spatially evolving turbulent flows. They showed that it is possible to generate a synthesized turbulent time-evolving signal, in which the prescription of a phase shift between different time steps allows to obtain a synthesized velocity field at the inlet featuring correct temporal correlations. One remarkable advantage of such a method is that the generation of the turbulent signal can be performed by using *Fast Fourier Transform - FFT* algorithms, which are computationally very efficient. The capability of generating an anisotropic random signal was introduced by Le et al. (1997). Based on the method of Lee et al. (1992), an isotropic turbulent synthesized signal is generated and then re-scaled using Eq.(2). In this way the reconstructed fluctuations match a prescribed Reynolds stress tensor. However, if one is interested in initializing the whole computational domain, the method may present some limitations. Indeed, since it is based on direct and inverse transforms using FFT algorithms, its application to non-uniform grids is possible at the inlet plane only, which considerably reduces its interest for practical applications.

More recently, Smirnov et al. (2001) modified the method of Le et al. (1997) in such a manner that it becomes possible to obtain a turbulent velocity field by requiring statistical information only. The method of Smirnov et al. (2001) is capable of synthesizing non-homogeneous turbulence within a general framework. It relies on the Fourier decomposition, with Fourier coefficients computed from spectral data based on local turbulent time and length scales obtained at

different locations across the flow. This method, called *Random Flow Generation* and denoted RFG hereafter, differs from the original proposal of Lee et al. (1992) since it does not make use of Fourier transforms. It is based on scaling and coordinates transformation operations only, which, on non-uniform grids, are much more efficient.

The RFG computational routines used here are detailed in Smirnov (2004) and a brief description of the procedure retained to generate the turbulent inflow data is now provided. According to Smirnov et al. (2001), a three-dimensional transient flow field, $u_i(x_j, t)$, can be obtained from,

$$u_i(x_j,t) = \sqrt{\frac{2}{n=N}} \sum_{n=1}^{N} \left[p_i^n \cos\left(\hat{k}_j^n \hat{x}_j + \omega_n \hat{t}\right) + q_i^n \sin\left(\hat{k}_j^n \hat{x}_j + \omega^n \hat{t}\right)\right], \quad (6)$$

where the following non-dimensional quantities have been introduced, $\hat{x}_j = x_j/l_t$; $\hat{t} = t/\tau_t$; $c = l_t/\tau_t$; $\hat{k}_j^n \hat{x}_j = k_j^n \hat{x}_j c/c_{(j)}$, where, $p_i^n = \varepsilon_{ijm}\zeta_i^n k_m^n$; $q_i^n = \varepsilon_{ijm}\xi_i^n k_m^n$, with, $\zeta_i^n, \xi_i^n, \omega_n \in N(0,1)$, $k_i^n \in N(0,1/2)$. Note that $N(M,\sigma)$ denotes a normal distribution with mean M and standard deviation σ. Repeated sub-indexes imply summation, following Einstein's rule, while parentheses around indexes preclude summation. In these non-dimensional expressions, l_t and τ_t denote the characteristic length and time scales of turbulence, respectively, ε_{ijk} is the permutation tensor used in the vector product operation, c_i denotes the fluctuating velocity components written in a new system of coordinates, which is obtained after the application of the transformation tensor a_{ij}. The numbers k_j^n, ω^n represent a sample of n wave-number vectors and frequencies of a modeled turbulence spectrum $E(k) = 16(2/\pi)^{1/2}k^4 \exp(-2k^2)$. The final flow field u_i is obtained after scaling and orthogonal transformation operations: $u_i = a_{ij}w_j$, where $w_j = c_{(j)}v_{(j)}$. It is important to note that the tensor a_{ij} is such that $a_{mi}a_{nj}R_{ij} = \delta_{mn}c_{(n)}^2$, and $a_{ik}a_{kj} = \delta_{ij}$, where R_{ij} is a prescribed velocity correlation tensor, e.g., the Reynolds stress tensor. It is also worth noting that this procedure requires specifying the characteristic integral length and time scales of turbulence, and the correlation tensor R_{ij} of the flow. These quantities can be obtained from experimental data, but some of them may also be approximated from preliminary RANS simulations. A

similar framework has been retained by Batten et al. (2004) to address the couplings between RANS and LES closures. This strategy has been applied with some success to the computation of a turbulent channel flow by Keating et al. (2004). The corresponding numerical simulation has been conducted with $N = 200$ Fourier modes, see Eq.(6), and a relatively long transition region has been required to regenerate fully-developped turbulence downstream of the inlet. Finally, assuming a modified von Kármán spectrum, a similar methodology has been also proposed by Davidson and Billson (2004) to generate *forcing conditions* at the matching boundary between the LES and URANS regions of hybrid numerical simulations. There is still today a fast-growing literature on the interfacing between RANS and LES methods and the present manuscript does not allow us to review it in further detail. The interested reader may find a rather complete view of this topic in the survey chapter of the book of Sagaut et al. (2006) and references therein.

2.2.4. Synthetic eddy method - SEM

The synthetic eddy method (SEM), proposed by Jarrin et al. (2009), is based on the decomposition of the turbulent flow field into stochastic coherent structures. The corresponding eddy-structures are generated at the computational domain inlet plane and defined thanks to a shape-function $f_\sigma(x)$, which is intended to encode turbulence spatial and temporal characteristics.

The SEM can be introduced using a one-dimensional scheme, in which the velocity component is generated within the range $[a, b]$. The shape-function of each turbulent spot features a compact support in $[-\sigma, \sigma]$ and it satisfies the normalization condition.

$$\frac{1}{\Delta} \int_{-\Delta/2}^{\Delta/2} f_\sigma^2(x) dx = 1, \tag{7}$$

where $\Delta = b - a + 2\sigma$. Each turbulent spot has a position $x^{(n)}$, a length scale σ and is assigned a signal $\epsilon^{(n)}$. In other words, the contribution $u^{(n)}(x)$ of a turbulent spot n to the velocity field, is defined as $u^{(n)}(x) = \epsilon^{(n)} f_\sigma(x - x^{(n)})$, with a location $x^{(n)}$ randomly chosen within the range $[a - \sigma, b + \sigma]$ and where $\epsilon^{(n)}$

denotes a random step of value -1 or $+1$. The synthetic eddies are generated in an interval larger than $[a, b]$. This larger interval guarantees that the inlet points are surrounded by eddies. Finally, the resulting velocity field $u(x)$ at any location will be the sum of the contributions of all synthetic eddies located in the domain, $u(x) = \sum_{n=1}^{n=N} \epsilon^{(n)} f_\sigma(x - x^{(n)})/\sqrt{N}$, where N denotes the total number of synthetic eddies. In three-dimensional situations, the generated eddies correspond to three-dimensional structures, which feature a compact support $[-\sigma_{x_1}, \sigma_{x_1}] \times [-\sigma_{x_2}, \sigma_{x_2}] \times [-\sigma_{x_3}, \sigma_{x_3}]$, and satisfy a normalization condition similar to Eq. (7). Considering an inlet plane of dimensions $[0, L_{x_2}] \times [0, L_{x_3}]$, located at $x_1 = 0$, the position $\left(x_1^{(n)}, x_2^{(n)}, x_3^{(n)}\right)$ of the synthetic eddy n is randomly chosen within $[-\sigma_{x_1}, \sigma_{x_1}] \times [-\sigma_{x_2}, L_{x_2} + \sigma_{x_2}] \times [-\sigma_{x_3}, L_{x_3} + \sigma_{x_3}]$. The eddies are convected through the inlet plane at a velocity U_0 obtained from Taylor's hypothesis $x_1^{(n)}(t + \Delta t) = x_1^{(n)}(t) + U_0\, \Delta t$. Once $x_1^{(n)}(t + \Delta t) > \sigma_{x_1}$, the eddy is re-generated at $x_1 = -\sigma_{x_1}$, and can be convected again. Finally the fluctuating velocity field is given by $u'_j(\boldsymbol{x}, t) = \sum_{n=1}^{n=N} \epsilon_j^{(n)} f_j(\boldsymbol{x} - \boldsymbol{x}^{(n)}(t))/\sqrt{N}$, where $\epsilon_j^{(n)}$ corresponds to the signal, i.e. -1 or $+1$, of the eddy n in direction j. The final velocity field u_i is then obtained from the above synthetic fluctuating velocity field u'_j, the velocity mean profile $\widetilde{u}_i$, and the Cholesky's decomposition a_{ij} of the Reynolds stress tensor: $u_i = \widetilde{u}_i + a_{ij} u'_j$, with a_{ij} defined by Eq. (2).

3. Mathematical and computational modelling

The mathematical and computational framework retained to proceed with the numerical simulation is now briefly presented. The interested reader may find a detailed presentation elsewhere (Vedovoto et al., 2011). A hybrid approach in which the LES methodology is coupled with the transport of the scalar probability density function (PDF) is retained to describe the reactive cases. The method involves the numerical solution of partial differential equations (LES solver) together with stochastic differential equations (PDF solver). From the LES approach the Eulerian filtered variables are evaluated while stochastic differential equations (SDE) are solved using Lagrangian notional particles to

simulate the modelled transport equation of the scalar PDF (Pope, 1985; Colucci et al., 1998). The latter yields the one-point, one-time statistics of subgrid-scale scalar fluctuations and thus provides the LES solver with the corresponding filtered chemical reaction rate.

3.1. Mathematical model

The present section is organized as follows: the filtered set of balance equations that describes the flows under consideration is first presented. The main characteristics of the transported PDF method are then briefly introduced together with the equivalent system of stochastic differential equations as well as the coupling between the Eulerian and Lagrangian approaches (LES-PDF).

3.1.1. Set of filtered equations

The following simplifying assumptions are used: (a) fluid is considered as Newtonian, (b) body forces, heat transport by radiation, Soret and Dufour effects are not addressed, (c) the model is developed for low Mach number flows, (d) we consider unity Lewis number values and equal molecular diffusion coefficients for all species, (e) heat losses are neglected. The mathematical model considers multi-species variable-density reactive flows, in which the primary transported variables are the density ρ, the three velocity components u_i, the specific enthalpy h and the mass fractions Y_k of the K chemical species ($k = 1, \ldots, K$), the balance equations are:

$$\frac{\partial \overline{\rho}}{\partial t} + \frac{\partial \overline{\rho}\,\widetilde{u}_j}{\partial x_j} = 0, \tag{8}$$

$$\frac{\partial \overline{\rho}\,\widetilde{u}_i}{\partial t} + \frac{\partial \overline{\rho}\,\widetilde{u}_j\,\widetilde{u}_i}{\partial x_j} = \frac{\partial \overline{T}_{ij}}{\partial x_j} - \frac{\partial \tau_{ij}^{SGS}}{\partial x_j}, \tag{9}$$

$$\frac{\partial \overline{\rho}\,\widetilde{\phi}_\alpha}{\partial t} + \frac{\partial \overline{\rho}\,\widetilde{u}_j\,\widetilde{\phi}_\alpha}{\partial x_j} = \frac{\partial \overline{Q}_{\alpha,j}}{\partial x_j} - \frac{\partial Q_{\alpha,j}^{SGS}}{\partial x_j} + \overline{S}_\alpha, \tag{10}$$

where the variable ϕ_α denotes the mass fraction of a chemical species or the enthalpy of the mixture, ($x_i, i = 1, 2, 3$) are the spatial coordinate, and t is the time. $T_{ij} = \tau_{ij} - p\,\delta_{ij}$ is the tensor of mechanical constraints including both a deviatoric (shear stresses τ_{ij}) and a spheric (pressure $p\,\delta_{ij}$) contribution, while

$Q_{\alpha,j}$ denotes the component of the molecular diffusion flux of the scalar α in the direction j. In the above expression, $\tau_{ij}^{SGS} = (\overline{\rho u_i u_j} - \overline{\rho}\,\widetilde{u}_i\,\widetilde{u}_j)$ is the subgrid scale (SGS) stress tensor and $Q_{\alpha,j}^{SGS} = \left(\overline{\rho u_i \phi_\alpha} - \overline{\rho}\,\widetilde{u}_i\,\widetilde{\phi}_\alpha\right)$ represents the SGS scalar flux components, respectively. Finally, the last term in the RHS of Eq. (10), i.e. $\overline{S}_\alpha$, denotes the filtered reaction rate. The above system is completed by an equation of state: $P = P_0(t) + p(\mathbf{x}, t)$, with $P_0(t)$ the thermodynamic pressure.

The unresolved momentum fluxes are expressed according to the Boussinesq assumption, $\tau_{ij}^{SGS} - \delta_{ij}\tau_{kk}^{SGS}/3 = 2\mu_{SGS}\left(\widetilde{S}_{ij} - \delta_{ij}\widetilde{S}_{kk}/3\right)$, where μ_{SGS} is the subgrid scale viscosity, and $\widetilde{S}_{ij} = (\partial\widetilde{u}_i/\partial x_j + \partial\widetilde{u}_j/\partial x_i)/2$ is the strain rate tensor of the resolved field (Ferziger and Peric, 1996; Fureby, 2008). In most of the numerical simulation results presented below, the eddy viscosity μ_{SGS} is obtained from the Smagorinsky closure, i.e., assuming that the small scales are in equilibrium, so that energy production and dissipation are in balance, which yields, $\mu_{SGS} = \bar{\rho}(C_s\Delta)^2|\widetilde{S}| = \bar{\rho}(C_s\Delta)^2\left(2\widetilde{S}_{ij}\widetilde{S}_{ij}\right)^{1/2}$, where C_s denotes the Smagorinsky constant. It is known that this closure can be excessively dissipative, especially near the walls, which is corrected herein by using a van Driest damping function (Ferziger and Peric, 1996). Finally, the SGS scalar flux is represented with a gradient law, $Q_{\alpha,j} = -\bar{\rho}\Gamma_{SGS}\partial\widetilde{\phi}_\alpha/\partial x_j$, where $\widetilde{\phi}_\alpha$ is the resolved scalar field and Γ_{SGS} denotes the subgrid diffusion coefficient evaluated from $\Gamma_{SGS} = \bar{\rho}(C_s\Delta)^2|\widetilde{S}|/Sc_{SGS}$ with Sc_{SGS} a subgrid scale turbulent Schmidt number.

The accurate determination of the filtered chemical reaction rate $\overline{S}_\alpha$ remains one of the most important challenges when applying LES to turbulent reactive flows. We retain herein a formulation that accounts for the subgrid scale fluctuations of the chemical composition through a modelled transport equation for the subgrid scale PDF, which provides an effective resolution to the closure problems that arise from averaging or filtering the highly nonlinear chemical source terms (Haworth, 2010). Since one-point one-time PDF models are used, the terms that involve two points information, i.e., some property gradients, are not explicitly resolved, hence important effects, such as molecular diffusion and

viscous effects, and associated dissipation phenomena require to be modeled.

The modelled transport equation for the scalar PDF is written as:

$$\begin{aligned}\frac{\partial}{\partial t}\rho(\Psi)P_\Phi(\Psi;\mathbf{x},t) &+ \frac{\partial}{\partial x_j}\rho(\Psi)\widetilde{u}_j P_\Phi(\Psi;\mathbf{x},t)\\ &= \frac{\partial}{\partial x_j}\left[\rho(\Psi)(\Gamma+\Gamma_{SGS})\frac{\partial P_\Phi(\Psi;\mathbf{x},t)}{\partial x_j}\right]\\ &+ \frac{\partial}{\partial \psi_\alpha}\left[\rho(\Psi)\Omega_m(\psi_\alpha-\langle\phi_\alpha\rangle)P_\Phi(\Psi;\mathbf{x},t)\right]\\ &- \frac{\partial}{\partial \psi_\alpha}\left[S_\alpha(\Psi)P_\Phi(\Psi;\mathbf{x},t)\right], \end{aligned} \tag{11}$$

where the chemical reaction term appears in closed form, thus circumventing the difficulties associated with the physical modelling of its filtered contribution. The derivation of such a transport equation may be found elsewhere (Haworth, 2010). The retained hypotheses are: (i) the conditional filtered velocity has been decomposed into filtered and subgrid contributions, with the latter closed by a turbulent diffusivity approximation, (ii) the conditional mixing term is closed by the IEM mixing model Villermaux and Devillon (1972) also often referred to as the linear mean-square estimation (LMSE) model (Dopazo and O'Brien, 1974). In the above equation, $\Omega_m = C_\omega(\Gamma+\Gamma_{SGS})/\Delta^2$ denotes the turbulent mixing frequency, with $C_\omega = 2.0$ the mechanical to scalar time scale ratio (Raman, 2004).

3.1.2. Lagrangian Monte Carlo approach

The Lagrangian Monte Carlo approach offers the most classical framework to deal with the above PDF transport equation (Pope, 1985; Fox, 2003). In this approach, the joint scalar PDF is represented by an ensemble of notional particles (Fox, 2003), which evolve according to equivalent stochastic differential equations (SDE). A general framework to construct SDEs that are equivalent to the PDF transport equation is provided by Gardiner (2009).

In the present context, the SDEs that describe the trajectory of the particles in the physical space, $\mathbf{x}$, and in the sample space of the scalar field, Ψ, can be written as:

$$d\mathbf{x} = \left[\widetilde{\mathbf{u}}(\mathbf{x},t) + \frac{\partial \Gamma_{SGS}}{\partial x_i}\right]dt + \sqrt{2\Gamma_{SGS}}d\mathbf{W}(t), \tag{12}$$

$$d\Psi = \left[-\Omega_m \left(\Psi - \langle\Phi\rangle\right) + S(\Psi)/\rho(\Psi)\right] dt \tag{13}$$

where $\mathbf{W}(t)$ denotes the Wiener process, associated with a Gaussian random variable featuring zero mean value and a variance dt (Fox, 2003). The evolution of each notional particle occurs according to statistically independent increments $d\mathbf{W}(t)$, with a subgrid scale diffusion coefficient evaluated from the LES solver. The possible restrictions associated with the use of such an approach have been extensively discussed by Haworth (2010).

3.2. Numerical model

This section reports the essential features of the numerical solver *FLUIDS_3D* that has been used to conduct the numerical simulations reported hereafter. The reader may refer to Vedovoto et al. (2011) for further insights on the Eulerian solver.

3.2.1. Navier-Stokes equations (NSE) solver

The numerical method is based on a three-dimensional, conservative, staggered, finite-volume discretization (Ferziger and Peric, 1996). In the present work, a fully implicit scheme is retained, which requires the numerical resolution of a large algebraic system; the MSIP - Modified Strongly Implicit Procedure (Schneider and Zedan, 1981) is retained to this purpose.

In the low Mach number flows under consideration, the density is solely determined by the temperature and thermodynamic pressure fields P_0. The energy equation plays the role of an additional constraint on the velocity field, which is enforced by the dynamic pressure. This constraint acts onto the velocity field divergence, and it is related to the total derivative of the density, see Vedovoto et al. (2011). Once the pressure correction is evaluated, the velocity field can be updated.

The present numerical simulations are conducted with a central difference scheme (CDS) to represent the spatial derivatives. Time integration is performed using the backward difference scheme (BDF) with a CFL number value set to 0.5. Further information about the available discretization procedures, as

well as the verification of the numerical code developed can be found in Vedovoto et al. (2011).

3.2.2. Stochastic differential equations (SDE) solver

The Lagrangian stochastic particles move through the physical space independently of each other. They are assigned spatial coordinates and represent mass. Due to the stochastic nature of motion, the number of particles present in a given elementary volume changes in time. In order to prevent particle accumulations in computational cells, and to keep small computational cells from running empty, particles are ascribed a relative weight (Zhang and Haworth, 2004). Following Pope (1985), the SDEs are discretized resorting to a fractional step method. For instance, Eq.(12) is re-written as $dx_i = A(X(t))dt + B(X(t))dW_i(t)$. The stochastic nature of this equation is associated with the Wiener process W_i. The increments of the Wiener process, $dW_i(t + \Delta t) = W_i(t + \Delta t) - W_i(t)$, with $i = 1, ..., N_w$, where N_w is the number of independent processes, drive the evolution of the particle in physical space. According to the model equation (11), the drift, $A(X(t))$, and diffusion coefficients, $B(X(t))$, are defined as, $A(X(t)) \equiv [\widetilde{u}_i + \partial(\Gamma + \Gamma_{SGS})/\partial x_i]$, and, $B(X(t)) \equiv \sqrt{2(\Gamma + \Gamma_{SGS})}$. The most widespread discretization procedure retained for such equations is the Euler-Maruyama method (Gardiner, 2009). However, such a method, in its explicit formulation, requires very small time steps due to stability issues. The present numerical simulations rely on the Milstein scheme (Kloeden and Platen, 2000) which has a strong and weak order of convergence equal to unity. Applying the Milstein scheme to Eq.(12) gives rise to the following discretized form $dx_i = A(X(t))\Delta t + B(X(t))\Delta W_i + 0.5\, B'(X(t))B(X(t))((\Delta W_i)^2 - \Delta t)$, where $B'(X(t))$ is the first derivative of $B(X(t))$ with respect to time.

3.3. Implementation of the synthetic turbulence generators. Discussion.

Four distinct turbulence generators have been implemented in the Navier-Stokes solver *FLUIDS_3D*. Among them, the simplest and still most widely-

used WN model simply consists in superimposing a white noise onto the mean velocity profile. However, its low computational cost and ease of implementation unfortunately cannot compensate for its poor representativeness, mainly due to its lack of energy at small wavenumbers, which may postpone any transition to turbulence.

As far as more realistic synthetized turbulence procedures are concerned, we will now discuss and compare the ease of both implementation and use of the DF, RFG and SEM procedures. The first method, i.e., the DF model, has been implemented from scratch in the *FLUIDS_3D* solver. It obviously demands a little bit more programming skills than those required to encode the WN model. However, its practical use remains quite simple provided that a detailed preliminary analysis of the sensitivity to the filter support size is conducted for the geometry of interest. In comparison with the WN model, it should be noted that the DF, RFG and SEM models all require to be fed with the Reynolds stress tensor components. In terms of computational performance, the DF method suffers from an important CPU cost, which is the highest among the different method that have been considered. This CPU cost increases at the power N^3 with N the size of the filter support.

Since it has been performed on the basis of an original set of RFG routines written in C programming language, the practical implementation of the RFG method was rather simple. Special care must be taken to avoid any misuse of data types as soons as C and fortran exchanges are required. The method is of very simple use and, if we except the WN model, it was found the most efficient among those implemented. It is worth recalling that all simulations carried out in this work make use of parallel processing. This is a quite important point since the CPU costs of the synthetic turbulence procedures used at the inlet of the computational domain may indeed lead to important unbalanced loads. This is a serious issue with respect to the use of the DF method. It has been noticed that, with the DF method, the computational sub-domains lying at the inlet require about 10 per cent more random access memory (RAM) than the others.

Finally, the last method considered is the SEM method. It has also been implemented from scratch in the *FLUIDS_3D* solver. In terms of complexity of implementation we must recognize that, given the amount of information available in the literature, this task is very affordable. The computational cost of the SEM is found comparable to the one of the RFG method. As shown and discussed later on, the capacity of generating an energy spectrum that mimics some desirable characteristics, such as an inertial zone featuring a $-5/3$ power-law decay rate as well as the capability of the SEM to recover a prescribed anisotropic tensor makes the method very appealing. In addition to this, the obtained results display only a rather small dependence on the number of eddies generated, which contributes to maintain the CPU costs reasonable.

4. Application to homogeneous isotropic turbulence

In the present brief section, we proceed with a preliminary inspection of the inflow generator capabilities for the case of a spatially decaying isotropic turbulence. The conditions studied herein are very similar to the ones previously considered by Jarrin et al. (2009) and the reader may refer to this archival publication for futher details. The mean flow is oriented towards the positive x_1-direction. The computational domain is a three-dimensional box with characteristic dimensions $(20 \times 6 \times 6)$, discretized with a finite volume mesh featuring $200 \times 60 \times 60$ cells in the x_1, x_2 and x_3-directions, respectively. The mesh is homogeneous in all three directions. Periodic boundary conditions are imposed along the x_2 and x_3-directions. An unsteady advective (also often denoted convective) boundary condition is applied on the outflow plane ($x_1 = 20$). This unsteady boundary condition determines a velocity field that ensures an outflow mass flux equal to the incoming mass flux. The implemented formulation is the one proposed by Orlanski (1976). The mean streamwise velocity is set to $U_0 = 20\, m/s$, and the molecular viscosity is $\nu = 3.5 \times 10^{-4}\, m^2/s$. The mean turbulent kinetic energy at the inlet is $k_0 = 3/2\ m^2/s^2$ and finally, for the simulation results presented below, the integral length scale is set to $L = 0.4\, m$.

It seems worth emphasizing that these values are exactly the same as those previously retained by Jarrin et al. (2009). Statistics are averaged over two flow-through domain times and over homogeneous periodic directions.

The set of results gathered in Fig. 1 displays the influence of the inflow turbulence generators. The energy spectra are extracted at five distinct locations in the computational domain. The five probes are located at $x_1 = 0.05$, i.e., in the first control volume immediately downstream of the inlet plane, and further downstream at positions $x_1 = 1$, $x_1 = 5$, $x_1 = 9$, and $x_1 = 19$. The x_2 and x_3-coordinates of the probes are held constant and equal to 3, i.e., positioned in the middle of the computational domain cross-section.

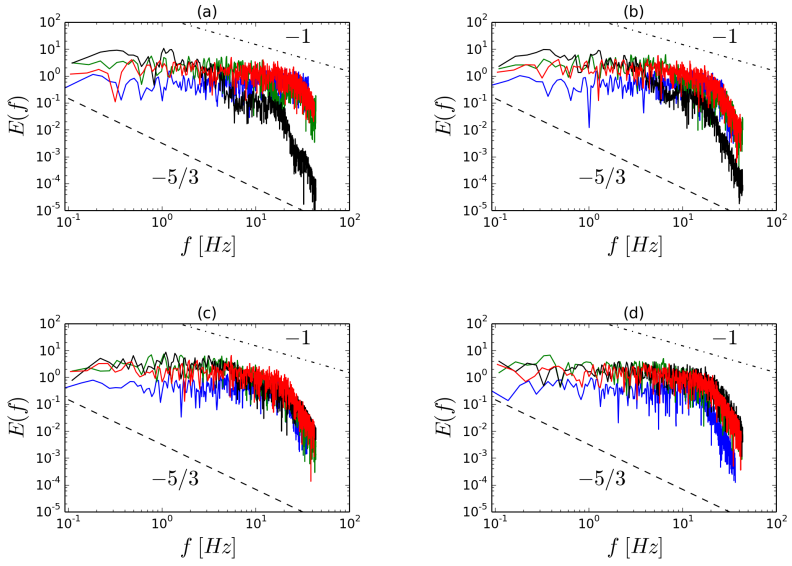

Figure 1: One-dimensional longitudinal energy spectra (u_1-component of velocity). The subfigures (a), (b), (c) and (d) correspond to the results of simulations obtained at $x_1 = 1$, $x_1 = 5$, $x_1 = 9$, and $x_1 = 19$ respectively. WN (blue curve); DF (green curve), RFG (black curve) and SEM (red curve).

To perform the comparative analysis, the white noise synthetic turbulence generator is considered with a fluctuation level of twenty per cent imposed on the

streamwise component of the velocity field, while 10 per cent fluctuations are set for the components in the x_2 and x_3-directions. For the simulations conducted with the DF method, the size of the filter support is set to 10 while $1,000$ Fourier modes are retained for the simulations based on the RFG method. For the simulation carried-out with the SEM, 10000 eddies are used. Time integration is performed using the Backward Difference Scheme with a CFL number value set to 0.5. The advective terms of the transport equations are discretized by using the CDS approach. Finally, since the numerical code developed has the capability of performing distributed computing, the computational domain is divided into 16 sub-domains.

From Fig. 1, it is clear that, for the probe positioned at $x_1 = 19$, the effects associated with the choice of one given inflow turbulence generator are minimized. At this position, the energy spectrum is indeed developed, i.e, the turbulent flowfield got enough time *to forget* the influence of the highest frequencies that were introduced through the synthetic inlet turbulence signals [1]. This offers quite a remarkable contrast with the spectra observed at the inlet ($x_1 = 0.05$) where strong differences may be observed and the effects of the inflow generator are very revealing. In fact, with the exception of the RFG model, it is worth noting that the different methods fail to display a satisfactory spectral behavior just downstream of the inlet. To conclude with this preliminary investigation, the values of the velocity derivative skewness are inspected, see Fig. 2. This quantity is related to vortex stretching and energy transfer. The value obtained at $x_1 = 19$ for the white noise is very small: $S = -0.030$. With the WN procedure all the energy is dissipated after a few cells downstream the inlet. The inflow data indeed does not exhibit any spatial and/or temporal correlation: two neighbouring points are uncorrelated, which leads to high velocity gradients and a quasi-instantaneous dissipation of turbulent kinetic energy at the inlet plane. This behavior simply confirms that the small computational cost of the WN model cannot compensate for its inability to reproduce even

[1] The obtained level of fluctuations still appears to be quite altered with the WN model.

the simplest statistics of the turbulent flow field. In contrast, we measured $S = -0.215$ at the same location ($x_1 = 19$) for the DF model, $S = -0.268$ for the RFG model and $S = 0.161$ for the SEM. Such values are comparable to those previously documented by Jarrin et al. (2009).

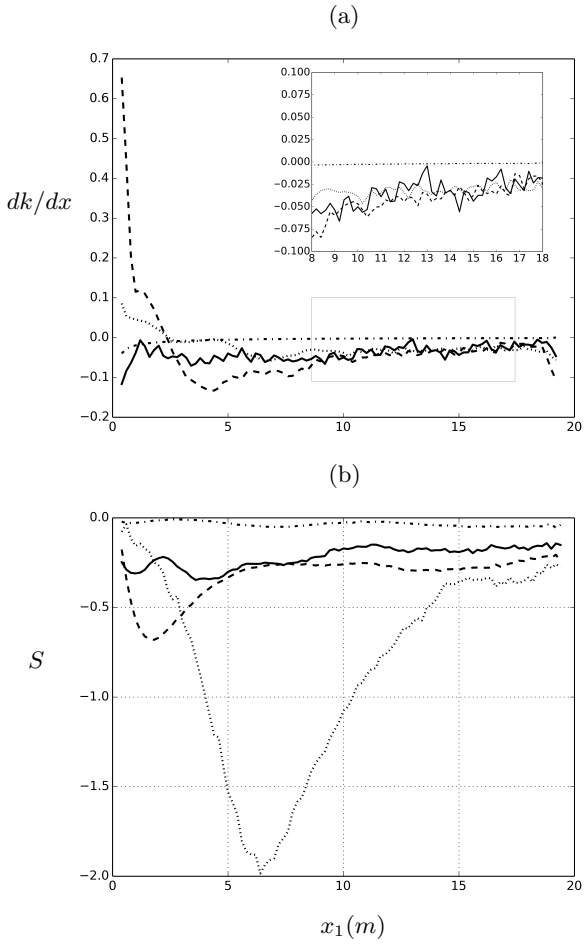

Figure 2: Downstream evolution of the (a) turbulent kinetic energy spatial decay rate (top), and (b) the velocity derivative skewness (bottom) plotted versus the longitudinal coordinate $x_1(m)$; (−.−) WN, (- -) DF, (..) RFG, and (—) SEM.

5. *A priori* analysis of the turbulent inflow data generators

The influence of turbulence inlet generators is now investigated in condi-

tions relevant to practical applications and we will compare resulting statistics in a simplified configuration so as to assess the efficiency of the models. Before examining the effect of the inflow generation technique on flowfields computed in a representative geometry, we present below comparative analyses of the implemented turbulent inflow data generators. The experimental stress tensor profile and mean velocity characteristics retained for testing the turbulent inflow generation techniques are based on the experimental studies conducted in the geometry of Moreau, see Magre et al. (1988). The corresponding experimental setup offers a reference test case (Bilger et al., 2005). For instance Andrade et al. (2011) performed the LES of the corresponding flowfield by resorting to a classical white noise generator and the present investigation may therefore be helpful to get a better understanding of the residual differences they observed between experiments and computational results. The experimental test section permits the development of a high speed turbulent mixing layer, where a premixed methane-air flow can be ignited and stabilized by a parallel stream of combustion products. Profiles of mean velocity, turbulence intensity and velocity fluctuations have been characterized for both reactive and non-reactive flows. Experimental data make available the R_{11} component of the Reynolds stress tensor only. Andrade et al. (2011), when simulating this configuration, assumed that the R_{22} and R_{33} components are approximately half of the R_{11} component. The components $R_{12} = R_{21}$ and $R_{32} = R_{23}$ are taken as zero. These assumptions are retained here. No information is given about the cross component R_{13}, but since it plays a crucial role in the shear layer spreading rate, we must satisfactorily approximate such a quantity. Brucker and Sarkar (2007) provide a relation in which the non-dimensional width of the shear layer, $\xi = h/\delta_m$, with h varying between $[-\delta_m < h < \delta_m]$, is correlated to the non-dimensional quantity $R_{13}/\Delta\bar{u}_1^2$ in self-similar mixing layers. Once defined the velocity difference between two streams, $\Delta\bar{u}_1^2$, and the width of the mixing layer $\delta_m = 5$ mm, the component $R_{13} = R_{31}$ can be evaluated from Brucker and Sarkar (2007) data.

The combustion chamber is a channel with dimensions $800 \times 100 \times 100\ mm^3$

in the directions x_1, x_2 and x_3 respectively. The inlet is divided into two ducts separated by a splitter plate. The fresh gases are injected at 65 m/s in the main (upper) duct while hot gases, featuring a mean velocity of 130 m/s, are injected in an auxialiary duct, see Fig. 3. For the present test, which aims at evaluating the variables of interest at the inlet plane only, the two-dimensional grid is divided into 50 points in the x_2-direction and 50 points in the x_3-direction. The mean velocity profile used at the inlet is represented by a combination of two developed flows at different exit velocities. The analytical function adopted for generating the corresponding mean velocity profile is,

$$\widetilde{u}_1(x_3) = C_{in}\left[1 - \left(\frac{x_3 - (a/2+h)}{a/2}\right)^{\gamma_{in}}\right], \tag{14}$$

where C_{in} is the mean value of the velocity in the duct, a is the position of the bottom part of the duct in the x_3-direction, h is the height of the duct, and γ_{in} is a constant that sets the thickness of the shear layer. The values of the above parameters are summarized in Table (1).

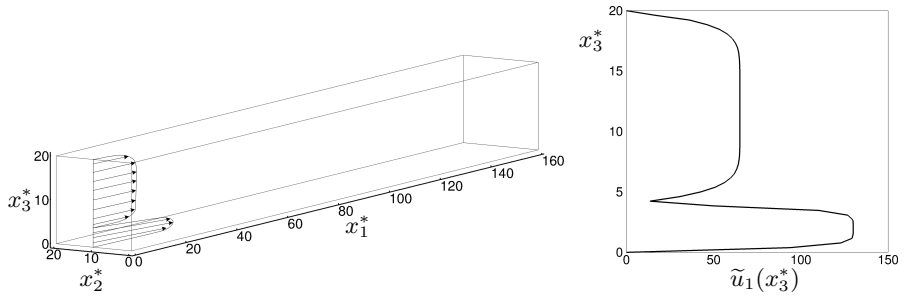

Figure 3: Computational domain retained to perform the numerical simulations (left), and mean velocity profile imposed at its inlet (right); $x_3^* = x_3/\delta_m$ denotes the non-dimensional coordinate with δ_m the initial width of the mixing layer

As stressed above, it is important to verify if the procedures implemented for generating the turbulent inflow data reproduce a random signal in which the energy spectrum distribution corresponds to more energetic scales in the smallest wave numbers, and to less energetic scales in the highest wave numbers.

Moreover, the capability to generate a prescribed Reynolds stress tensor is also of paramount importance.

Table 1: Values of the parameters associated with the imposed mean velocity profile.

Duct	C_{in} [m/s]	h [m]	a [m]	γ_{in}
Main duct	65	0.02	0.08	6.0
Auxiliary duct	130	0.00	0.02	8.0

The DF and RFG methods feature some factors that directly impact both the accuracy in reproducing the characteristics of the flows of interest and the associated computational cost. Concerning the former, the main factor is the filter support size, and for the latter, i.e., the RFG method, the number of Fourier modes in Eq. (6). For the SEM, the number of eddies may be expected to be the critical parameter. Given a set of initial conditions, e.g., mean velocity distribution, size and number of control volumes of the computational domain at the inlet, Reynolds stress tensor, characteristic length and time scales of a flow, the turbulent inflow generators are used to recover the statistics of the flow properties of interest by a classical averaging procedure applied on 5000 samples. In the present work, to reduce the computational cost, an isotropic signal is generated, and then Eqs. (1) and (2) are applied to the resulting signal in order to obtain the desired level of anisotropy.

5.1. WN model

The first and simplest method is the superimposition of a white noise on the mean velocity profile given by Eq. (14). In this case, a random signal with zero mean and unity variance is adjusted to yield fluctuations representing 20 per cent of the mean velocity in the x_1-direction of the flow, i.e., the u_1-component of velocity. In the x_2 and x_3-directions, the fluctuations levels are set to 10 per cent of the mean velocity. Figure 4 displays a one-point temporal spectrum obtained from the energy of velocity fluctuations, i.e., $k(t) = 1/2\left(u_1'^2(t) + u_2'^2(t) + u_3'^2(t)\right)$, which has been sampled from a probe placed in the middle of the inlet plane. Note that the corresponding samples

were selected in such a manner that they are equally-spaced in time and the frequency of data sampling has been optimized to restrict any possible loss of information. As illustrated in this figure, the fact that the energy is spread over the whole energy spectrum, whatever the fluctuation frequency, contradicts the classical Kolmogorov description of turbulent flows.

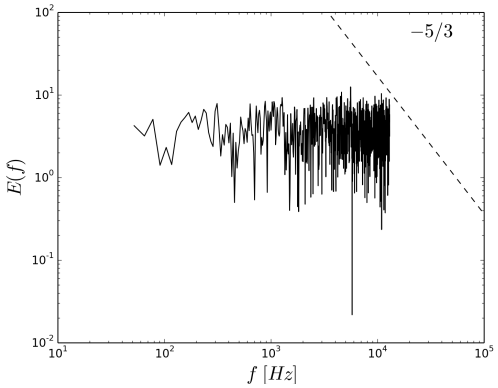

Figure 4: Energy spectrum associated with a WN generator.

As expected, the lack of spatial or temporal correlations, added to the isotropic nature of this process, leads to rather poor results when the components of the computational stress tensor, as evaluated from the averaging process of the inlet signal, are compared with experimental results, see Fig. 5. Therefore, it can be foreseen that the use of the WN technique will lead to poor results when applied to the full numerical simulation of the corresponding experimental benchmark.

5.2. DF model

With the DF method, we may expect a certain degree of dependency of the results on the filter support size. Since the filter size is directly connected to the number of grid points at the inlet, the computational cost associated with the number of points in the support, therefore, is an important issue. As it can

be seen in Fig. 6, as the support size is increased, the energy spectrum becomes more representative of the one associated with a fully developed turbulent flow.

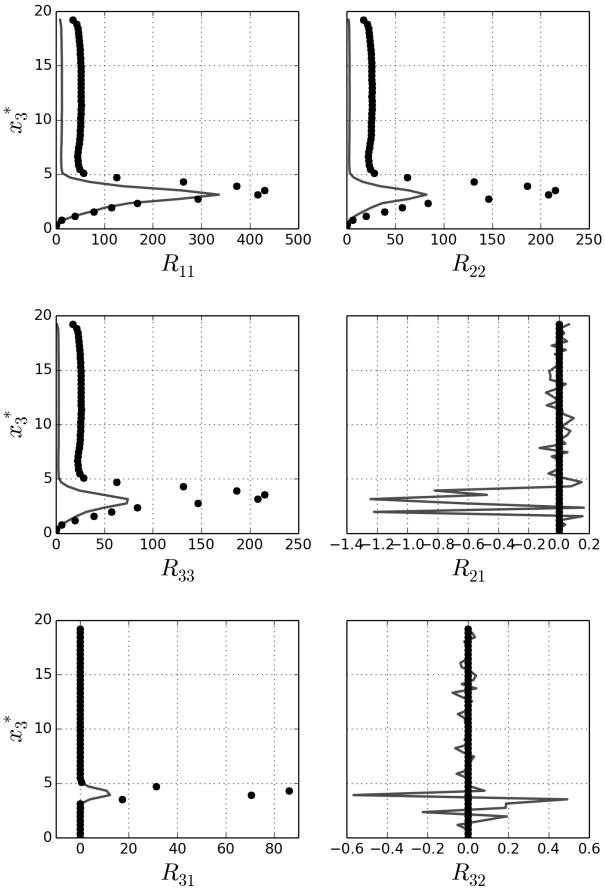

Figure 5: Stress tensor components evaluated from the white noise superimposition on the mean velocity profile; symbols •: experimental data from Moreau and Boutier (1977); line: WN results.

Within the DF framework, the filter support size and the integral length scale are interrelated through the expression of the filter coefficients b_j, and

as expected, with $N = 1$, the correlation is truncated to zero and the energy spectrum thus exhibits little difference from a white noise spectrum. The differences become more pronounced for N equal to 5, 10 and 20. For a given level of resolution, the influence of an increase in the filter support size is indeed similar to an increase of the turbulent length scale.

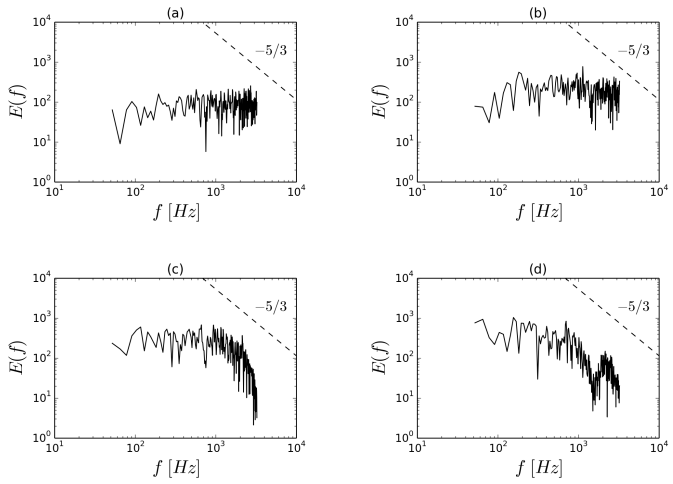

Figure 6: Influence of the support size N on the energy spectrum obtained with the DF method: (a) N=1, (b) N=5, (c) N=10, (d) N=20.

Concerning the computational cost of the DF method, in the tests carried out to evaluate the sensivity to the number of points N in the filter support, we obtain the following results: for $N = 1$, the code spent approximately one minute (using a CPU Intel (R) Xeon (TM) 3.00GHz with 4 gigabytes of RAM memory) to perform the 5000 iterations required to evaluate the statistics, whereas, for $N = 20$, for the same number of iterations, using the same computer, approximately 14 hours and 30 minutes were necessary.

Such a disparity can be easily understood by using a very simple example. For $N = 5$, a cubic box of dimensions $5 \times 5 \times 5$ is created for each point at the inlet. Since, in the present configuration, the inlet is composed of a grid of 50×50 points in x_2 and x_3-directions, respectively, the total number of points

where the filtering process is performed is $50 \cdot 50 \cdot (5 \cdot 5 \cdot 5)$, or, $312,500$ points. For $N = 20$ this number becomes $2{\times}10^7$ points, which is 64 times larger.

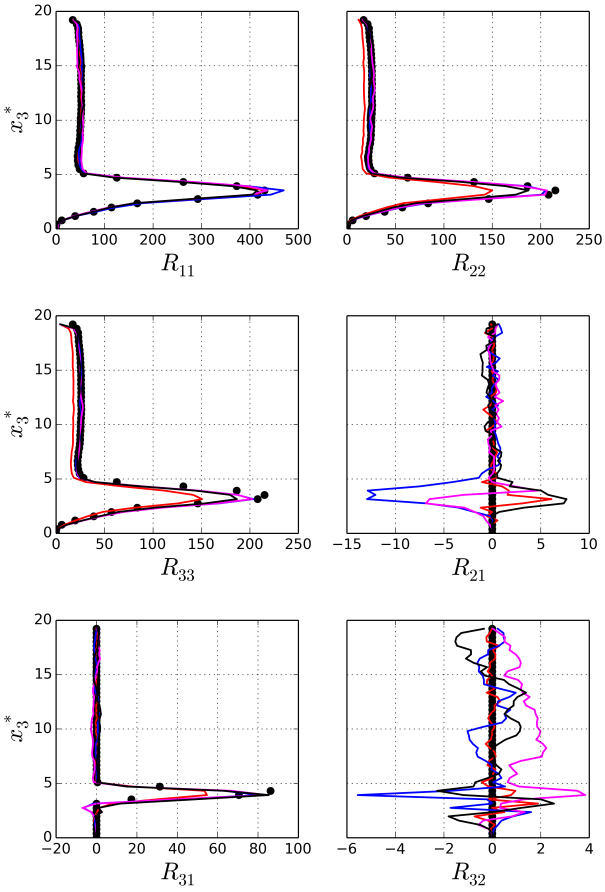

Figure 7: Stress tensor components evaluated from the DF method ; • experimental data from Moreau et al (1977); Red curve: N=1; Blue curve: N=5; Magenta curve: N=10 and Black curve: N=20

Concerning the capability of the DF method to reproduce anisotropic stress tensors, it can be seen in Fig. 7 that the support size influence is clearly less ob-

738 vious than the effects previously evidenced in the energy spectrum. It is indeed
739 observed that, for filter supports larger than 10 points, no further improvement
740 is obtained. From this preliminary analysis it is therefore suggested to retain a
741 support size of 10 points for the subsequent numerical simulations.

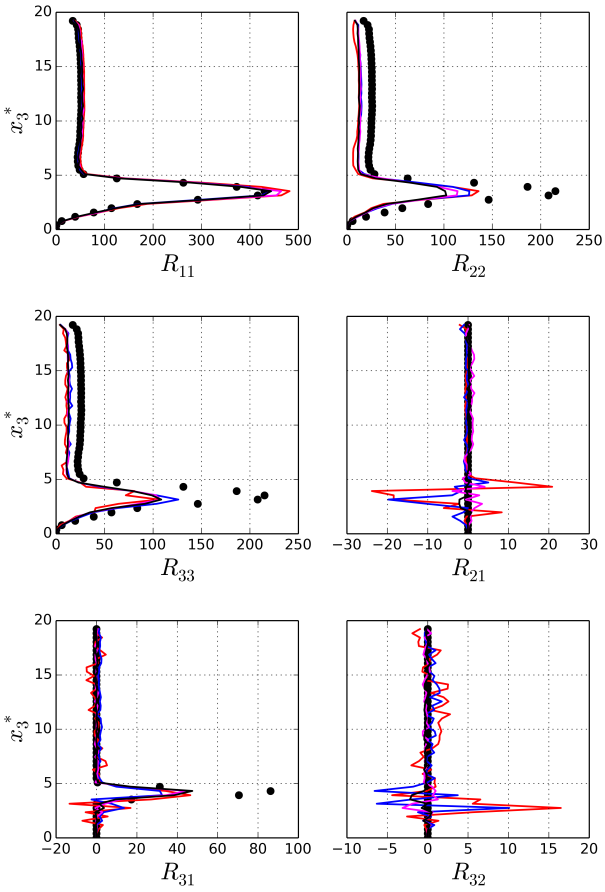

Figure 8: Stress tensor components evaluated from the RFG method, influence of the number of Fourier modes: • experimental data from Moreau and Boutier (1977); Red curve: 50 Fourier modes; Blue curve: 500 Fourier modes; Magenta curve: 1000 Fourier modes and Black curve: 5000 Fourier modes

5.3. RFG model

For the tests presented in the this section, the RFG model is not found to be very sensitive to the number of Fourier modes retained, in terms of its ability to reproduce the prescribed stress tensor, as well as the shape of a turbulent spectrum, as can be seen in Figs. (8) and (9), respectively. Note that N stands for the number of Fourier modes retained in one single direction, and the same number of modes is considered in the three directions.

When a turbulent flow is analyzed in terms of Fourier modes, each mode can be understood as a particular turbulent scale. From Fig. 8, it is confirmed that, even a small number of Fourier modes provides a satisfactory reproduction of the prescribed stress tensor. Above 500 Fourier modes the differences observed between experimental data and computational results become completely insignificant.

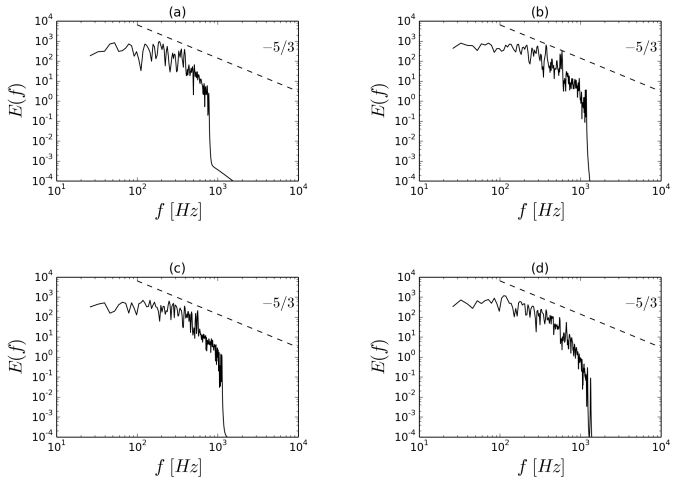

Figure 9: Influence of the number of Fourier modes on the energy spectrum obtained with RFG method: (a) 50 Fourier modes, (b) 500 Fourier modes, (c) 1000 Fourier modes and (d) 5000 Fourier modes.

It can be noted in Fig. 9 that, as the number of Fourier modes is increased, the energy spectrum becomes more representative of that associated with high

Reynolds number turbulent flows. Moreover, it is observed in Fig. 9 that only very slight differences persist when the number of Fourier modes exceeds $1,000$.

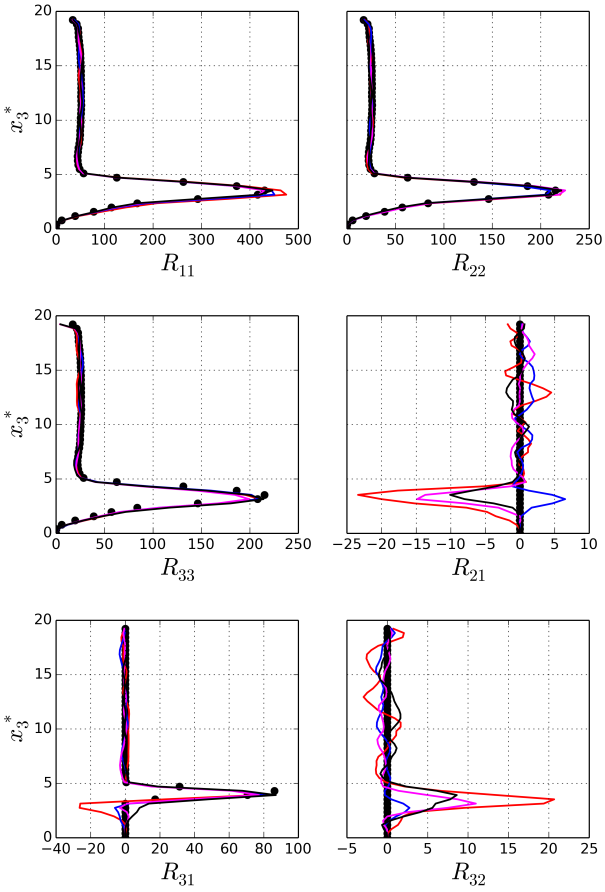

Figure 10: Stress tensor components evaluated from the SEM model; • experimental data from Moreau et al (1977); Red curve: 100 eddies; Blue curve: 1000 eddies; Magenta curve: 10000 eddies and Black curve: 100000 eddies

To conclude, we found that obtaining turbulent inflow data featuring representative energy spectra is computationally cheaper using the RFG model

than the DF model. For instance, the time spent to perform 5000 iterations, with $1,000$ Fourier modes for obtaining computational statistics comparable to experimental data, is approximately five minutes. This is similar to the time consumed by the DF method, with a support $N = 5$, on the same Intel (R) Xeon (TM) 3.00GHz CPU with 4 gigabytes of RAM memory. Therefore, the numerical simulations reported in the next sections are performed with $1,000$ Fourier modes.

5.4. SEM model

As emphasized in section 2.2.4, the results obtained with this method are expected to be sensitive to the turbulence characteristic length scale chosen. Such a quantity may be evaluated experimentally but, for the present application, this characteristic length scale is set to a constant value equal to $0.1\,m$. This value was also the input parameter of the RFG method in the previous section.

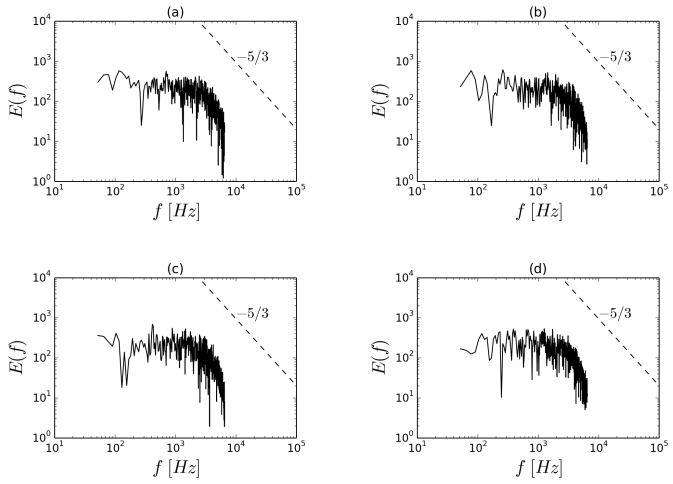

Figure 11: Comparison of the effects of the number of eddies on the shape of the energy spectrum obtained with the SEM model. (a) 100 eddies, (b) 1000 eddies, (c) 10000 eddies, (d) 100000 eddies.

The SEM is subject to the same preliminary tests as those applied to the

DF and RFG methods. We study the capability of correctly reproducing the Reynolds stress tensor, and examine the shape of the resulting turbulent energy spectrum. It is possible to verify in Fig. 10 that a satisfactory representation of the Reynolds stress tensor can be obtained whatever the number of eddies initially prescribed, even with a total number of eddies varied between 100 (0.1k) and 100,000 (100k) eddies. Such an independence on the total number of eddies is also evidenced in Fig. 11. Indeed, the energy spectrum does not seem to be influenced by the number of modes, provided that it is larger than 100.

The computational cost, however, is found to vary linearly with the number of eddies. For 100k eddies, for instance, to perform 5000 iterations (using the same Intel (R) Xeon (TM) 3.00GHz CPU with 4 gigabytes of RAM memory), the time spent was about six minutes, while for 1k eddies, the code requires about 3 seconds only. In comparison with the calculations performed with the RFG and DF methods, the SEM appears thus to be considerably cheaper.

In the next sections we proceed with the analysis of the different turbulent inflow generators by conducting the LES of the experimental test case of Moreau and coworkers. In a first step of the analysis, the corresponding wall bounded turbulent mixing layer flows is investigated in non-reactive conditions and then attention is focused on the high-speed turbulent and reactive mixing layer.

6. Application to the numerical simulations of a wall bounded turbulent mixing layer flow

6.1. Sensitivity to the synthetized turbulence model

In order to assess the influence of the synthetic turbulence generators, three-dimensional numerical simulations of a high speed mixing layer are now performed. The obtained results are compared with the experimental data. The computational domain is a three-dimensional box with dimensions $(800 \times 100 \times 100)$ mm^3, discretized with a finite volume mesh featuring $320 \times 100 \times 100$ cells in the x_1-, x_2- and x_3-direction, respectively. Since the numerical code developed has the capability of performing distributed computing, the computational do-

main is divided into 40 sub-domains. No-slip boundary conditions are imposed in the x_2 and x_3 directions. An advective boundary condition is used at the outflow. The Smagorinsky model is used with $C_s = 0.18$, and the Van-Driest damping function is applied at the walls. The Reynolds number, based on the initial width of the mixing layer, $\delta_m = 5$ mm, the mean velocity difference between the two inlet streams $U_r = 97.5$ m/s and the value of the kinematic viscosity of air at 600 K is $Re = 3075$.

To perform the comparative analysis, the white noise synthetic turbulence generator is considered with fluctuation levels of 20 per cent and 10 per cent imposed on the streamwise and transverse velocity components respectively. For the simulations conducted with the DF method the size of the filter support is set to 10, whereas $1,000$ Fourier modes are retained for the simulations based on the RFG method. For the simulation carried out using the SEM, $10k$ eddies are used. The mean velocity profile at the inlet is given by Eq. (14).

A probe is positioned just downstream of the computational domain inlet, in the first control volume along the x_1-direction, and at $x_2^* = 10$ and $x_3^* = 4.6$. In Fig. 12 the normalized longitudinal filtered velocity component, i.e., $u^* = u/U_r$, is plotted against the normalized time, i.e. $t^* = tU_r/\delta_m$. In this figure the presence of high frequency structures appears to be more pronounced for the white noise, while it is less apparent for the velocity signal evaluated from the method of Klein et al. (2003). Moreover, one can notice in Fig. 12-(c) that there are almost no high frequencies in the velocity signal, which can be explained by the lack of energy that has been evidenced at the small scales in the decaying part of the energy spectrum, see Fig. 6. The same conclusion applies to the SEM.

Figure (13) displays the time-averaged filtered turbulent kinetic energy (TKE), evaluated from the trace of the Reynolds stress tensor, for the different methods retained to generate the inflow. The statistics are obtained by time averaging the filtered flow field over four flow-through (residence) times, resulting in ap-

proximately $15,000$ realizations.

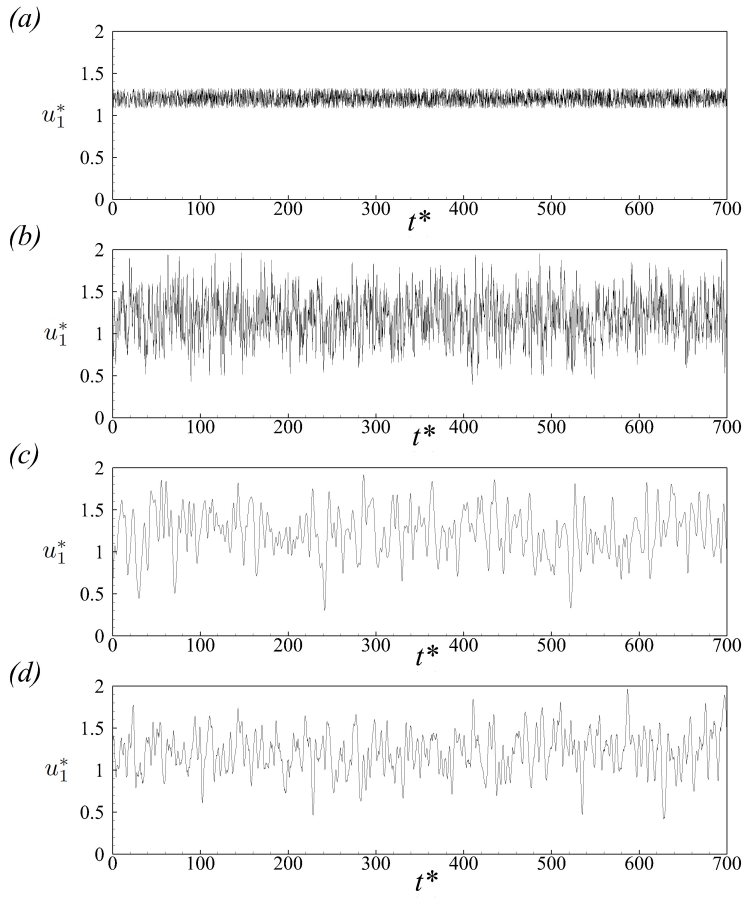

Figure 12: Temporal evolution of the u_1 component of velocity downstream of the flow inlet; (a) WN, (b) DF, (c) RFG, and (d) SEM.

It is noteworthy that the use of an improved method to generate the turbulent inflow data drastically changes the flow field structure. For instance, in Fig. 13-(a) the TKE levels become significant after one half of the total length of the computational domain in the x_1-direction only, whereas for the DF and RFG methods, the flow resembles that observed experimentally, see Fig. 13. Due to the high level of turbulent intensity in the incoming ducts that inject fresh

and burnt gases streams into the combustion chamber, the turbulence at the inlet is fully developed. It is worth noting that in the comparisons henceforth shown concerning the Reynolds stress tensor components, the sub-grid contribution is also accounted for. The turbulent kinetic energy levels for the DF, RFG and SEM are also larger downstream of the inlet of the computational domain. Again, although a transition to turbulence is observed when the white noise generator is used, practically all velocity fluctuations entering the computational domain are almost immediately dissipated close to the inlet boundary condition, and the first coherent structures are observed only after the first half length of the computational domain, along the x_1-direction.

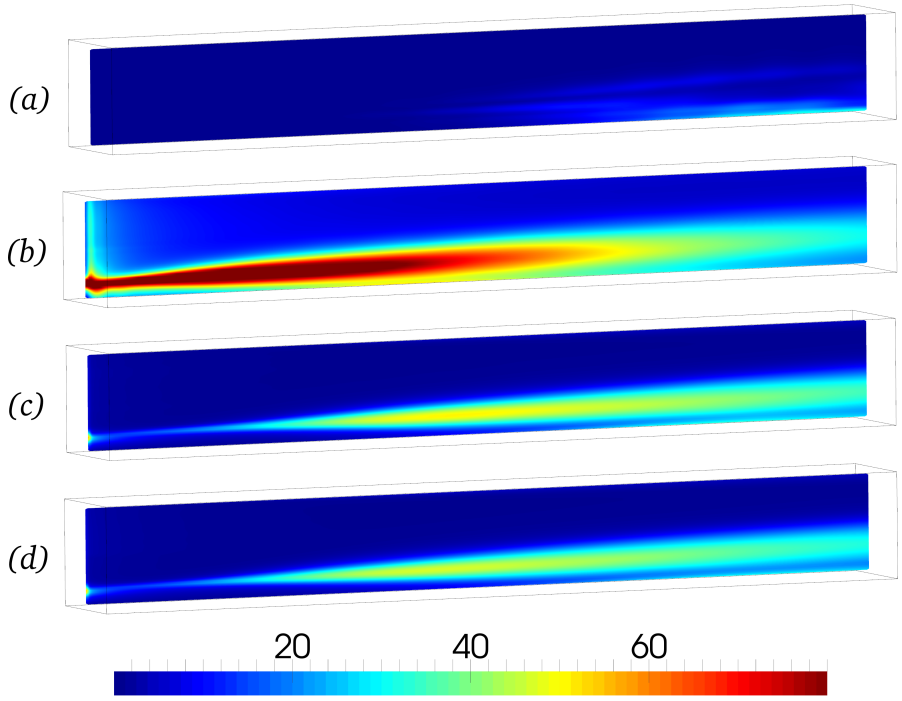

Figure 13: Fields of turbulent kinetic energy for the simulations carried out with the methods: (a) WN, (b) DF, (c) RFG and (d) SEM.

An instantaneous field of the normalized effective turbulent viscosity, i.e. $\mu_e^* = (1 + \mu_{SGS}/\mu)$, is reported in Fig. 14. It is clear from this figure that the

level of turbulence at the inflow is higher in sub-figures (b), (c), and (d). It can thus be concluded, that, since the Smagorinsky model is used, and since such model relies on the resolved strain rate to evaluate the sub-grid viscosity, the values of strain rate in the vicinity of the inlet of the computational domain is higher for the DF, RFG and SEM than when the white noise is considered.

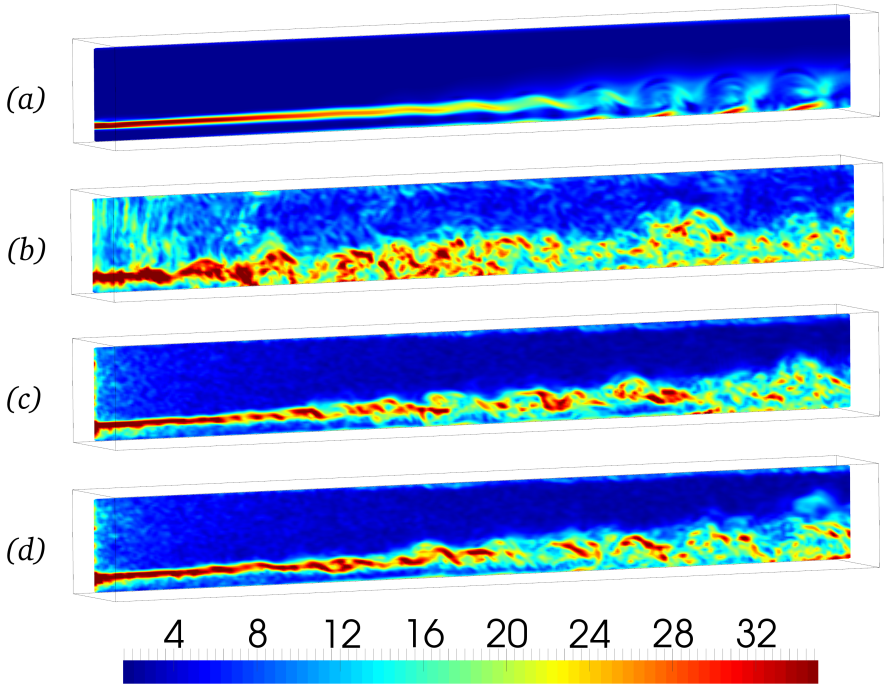

Figure 14: Snapshot of the normalized effective turbulent viscosity μ_e at $t^* = 19500$, for the simulations carried out with the methods: (a) WN, (b) DF, (c) RFG and (d) SEM at $t = 1s$ ($t^* = 19500$).

Figure 15 displays an isovalue of Q, the second invariant of the velocity gradient tensor, which is colored by the velocity magnitude. It shows clearly that the WN is subject to a transition in the middle of the computational domain. In comparison with the RFG and SEM, it is also evident from this figure that there is a more significant turbulent activity just downstream of the inlet plane when the DF method is used.

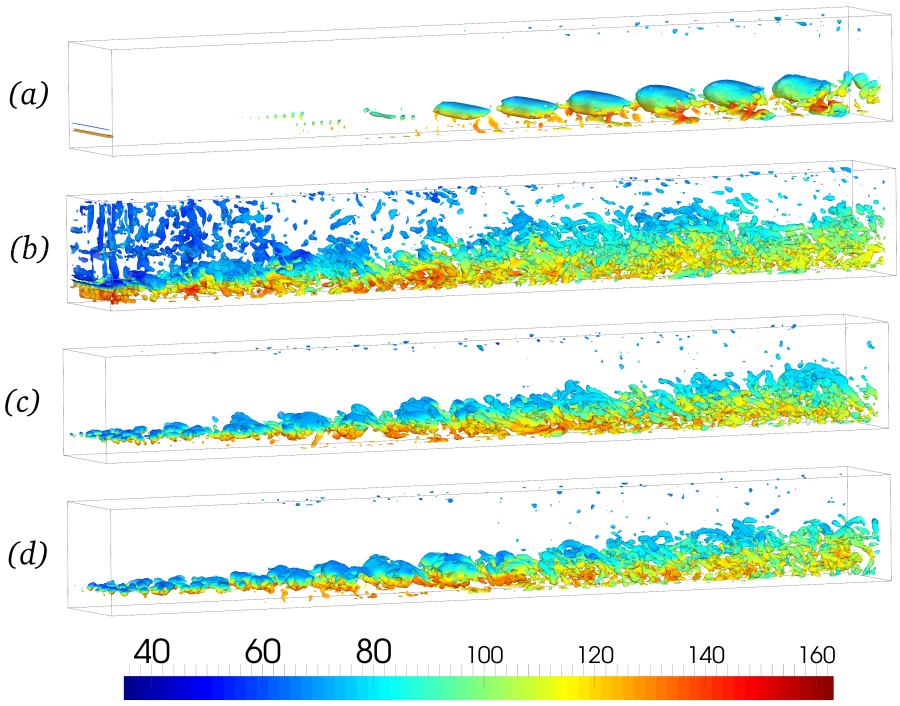

Figure 15: Iso values of $Q = 2.5 \times 10^6$ colored by the filtered velocity magnitude for the methods (a) WN, (b) DF, (c) RFG and (d) SEM at $t = 1s$ ($t^* = 19500$).

Figure 16, which depicts the vorticity component along direction x_2, also provides a valuable insight into the behavior of the Smagorinsky model. It is commonly agreed that the Smagorinsky model is highly dissipative. This is one of the reasons that also explains why the white noise generator signal imposed at the inlet may be rapidly destroyed. However, provided that a more elaborated method is retained to generate the inflow turbulence, Fig. 14 confirms that a signal featuring large scales introduced in the domain is not so quickly dissipated, even when the Smagorinsky model is used.

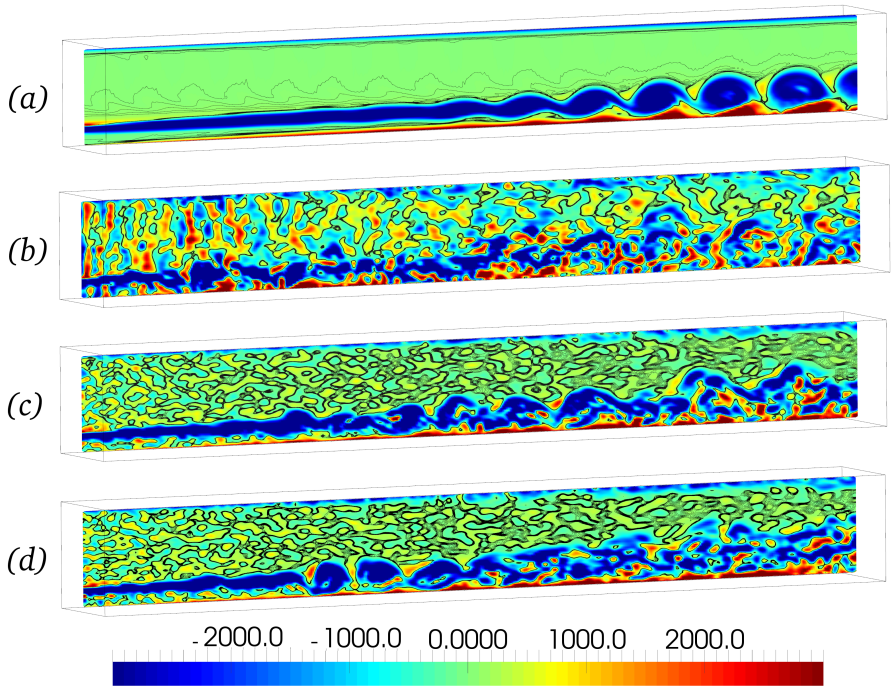

Figure 16: Component in x_2-direction of the vorticity as obtained from the simulations carried out with the methods (a) WN, (b) DF, (c) RFG and (d) SEM at $t = 1s$ ($t^* = 19500$).

In order to assess more quantitatively the methods implemented, Fig. 17 displays comparisons of the averaged u_1-component of the velocity with experimental data at four distinct locations in the computational domain, for $x_2^* = 10$. The results confirm that the different methods provide an acceptable representation of the mean velocity field when compared with experimental data. However the need for an improved turbulent inflow generator becomes clear to recover the levels of velocity fluctuations. Indeed, it can be seen in Fig. 18 that the superimposition of white noise on the mean velocity is unable to recover the experimental data in the first half of the computational domain along the x_1-direction - a conclusion that agrees with the previous work of Andrade et al. (2011). In contrast, the results obtained with the DF, RFG and SEM display a more satisfactory level of agreement with experimental data at the same loca-

tion. It is also worth noting the presence of two maximum values on the $\sqrt{R_{11}}$ profile, featuring a remarkable amplitude for the SEM. The first, positioned around $x_3^* = 5$, is associated with the shear layer growth, whereas the second develops in the vicinity of the wall.

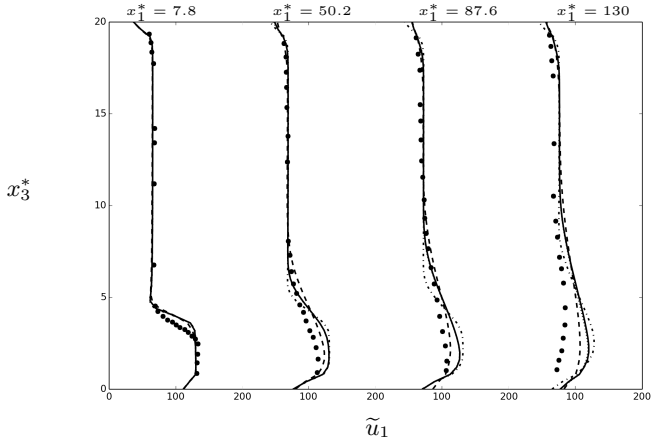

Figure 17: Mean longitudinal velocity profiles obtained using the classical Smagorinsky model. (•): Experimental data(−.−) WN, (- -) DF, (..) RFG and (—) SEM.

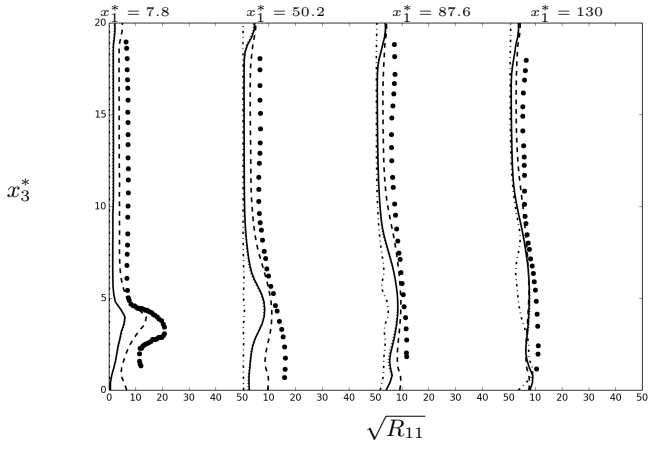

Figure 18: $\sqrt{R_{11}}$ stress tensor component profiles obtained using the classical Smagorinsky model. (•): Experimental data(−.−) WN, (- -) DF, (..) RFG and (—) SEM.

From the computational cost point of view, it is clear that the better quality of the results obtained with the DF, RFG and SEM methods requires a non-negligible amount of CPU time. For the present test case, the simulations conducted with the DF and RFG methods correspond to approximately the same computational cost, i.e., about 40 per cent more than that associated with the white noise methodology, for the former, and 35 per cent for the latter. The cost associated with the numerical simulations conducted with the SEM is 55 per cent higher than that conducted with the white noise. The DF and RFG methods therefore, appear as very attractive. Nevertheless, there are two crucial differences between the DF and RFG methods. The first does not yield temporal correlations, only spatial correlations are guaranteed. Moreover, the RFG method generates a divergence-free velocity field at the inlet. This confirms that the RFG method is an excellent candidate to impose synthesized turbulence.

6.2. Sensitivity to the SGS closure

Whatever the intrinsic qualities and limitations of the synthetic turbulence generators it should be acknowledged that the overly dissipative nature of the Smagorinsky model may significantly alter the comparison performed above between the computational results and the experimental data. It is therefore proposed in this subsection to analyze the different turbulence generators in conjunction with another subgrid-scale closure.

In practice, many solutions have been proposed to remedy the excessive dissipation of the standard Smagorinsky model. For instance, it has been combined with the similarity subgrid-scale model of Bardina et al. (1980) to obtain a *mixed* model, see Liu et al. (1994). Another solution consists in adjusting dynamically the Smagorinsky constant C_s to the flow conditions, following the procedure of Lilly (1992), *via* a double filtering in the physical space (Germano, 1992). The computational results obtained with such a dynamic Smagorinsky closure are compared to experimental data in Figs. 19 and 20. From a general point of view, it must be recognized that the quality of the agreement between

computations and experiments is only slightly improved. However, the use of the dynamic procedure produces significantly better results for the level of fluctuations obtained at $x_1 = 7.8$, see Fig. 20.

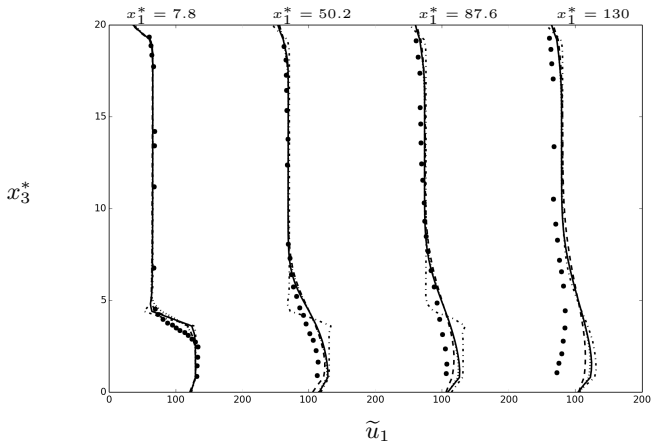

Figure 19: Mean longitudinal velocity profiles obtained using the dynamic Smagorinsky model. (•): Experimental data(−.−) WN, (- -) DF, (..) RFG and (—) SEM.

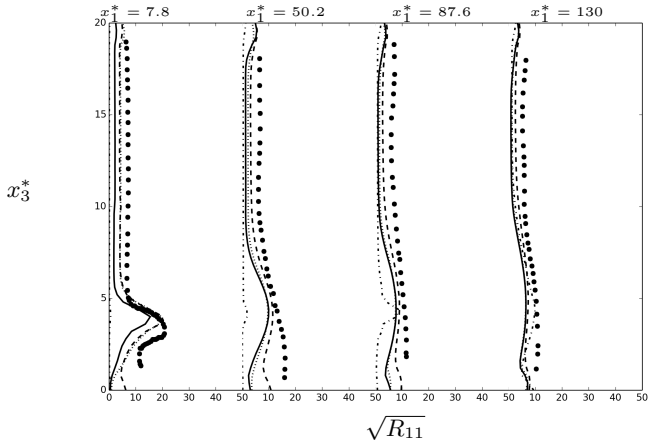

Figure 20: $\sqrt{R_{11}}$ stress tensor component profiles obtained using the dynamic Smagorinsky model. (•): Experimental data(−.−) WN, (- -) DF, (..) RFG and (—) SEM.

7. Reactive flows simulations

Although there is already some literature available to describe the importance of realistic turbulent inflow data prescription on non-reactive flows, such an analysis of the turbulent inflow data effects is much less common for turbulent reactive flows. In this last section, a set of two-dimensional reactive flow simulations is conducted to evidence such effects and then the paper ends with a tri-dimensional numerical simulation performed with the RFG synthetic turbulence model. The procedure followed here is identical to that adopted to impose the turbulent boundary conditions in non-reactive flows, i.e., a set of numerical simulations was carried out in order to evaluate the effects of the different methods for turbulent inflow generation: (*i*) superimposing white noise on the mean velocity profile (WN model), using (*ii*) the DF method, (*iii*) the RFG method and, finally, (*iv*) the SEM.

Table 2: Values for mean velocity profile retained for the simulation of reactive flows.

Duct	C_{in} [m/s]	h [m]	a [m]	γ_{in}
Main duct	55	0.02	0.08	6.0
Auxiliary duct	110	0.00	0.02	8.0

7.1. Two-dimensional numerical simulations

The computational domain is a three-dimensional box with dimensions ($800\times 2\times 100$) mm^3. It is discretized with a mesh of $320\times 1\times 100$ control volumes in the x_1, x_2 and x_3-direction, respectively. Periodicity and no-slip boundary conditions are imposed along x_2 the x_3-directions respectively. The computational domain is divided into 8 parallel regions. The other parameters remain the same as those retained for non-reactive cases. For the simulation conducted with the white noise, a fluctuation level of 20 per cent is imposed on the streamwise velocity component, while fluctuations of 10 per cent are set for the cross stream velocity component. For the simulations performed with the DF method of Klein et al. (2003) the filter support size is set to 10, while one

thousand $(1,000)$ Fourier modes are used for the simulations based on the RFG method of Smirnov et al. (2001). Ten thousands $(10k)$ eddies are considered in the simulation conducted with the Synthetic Eddy Method (SEM). Magre et al. (1988) have provided a large amount of experimental data gathered in the geometry previously used by Moreau and Boutier (1977) for different flow conditions. The mean velocity profile has the same shape as the one employed for the non-reactive flows, see Eq. (14). However, to be consistent with the measurements performed in reactive conditions by Magre et al. (1988), the mean velocity profile is parameterized with the values reported in Tab. (2).

To proceed with the mathematical modelling of the chemical source term, we retain a single step, global, and irreversible reaction that involves the progress variable, i.e., a normalized temperature defined by $c \equiv (T - T_u)/(T_b - T_u)$ where the subscripts u and b denote fresh reactants and fully burned gases conditions respectively. The corresponding chemical reaction rate is given by $S(c) = A_\alpha \rho \dot{\mathcal{S}}$, where the pre-exponential constant can be calculated as $A_\alpha = \Lambda S_L^2/[\alpha \exp(-\beta/\alpha)]$ and $\dot{\mathcal{S}} = (1-c)\exp[-\beta(1-c)/(1-\alpha(1-c))]$, see Williams (1985). In the previous expressions, α denotes a normalized temperature factor $\alpha = (T_b - T_u)/T_b$ and the reduced activation energy is $\beta = \alpha(T_a/T_b)$, where $T_a = E_a/R$ is the activation temperature, E_a is the activation energy and R is the universal constant of gases. Here, we set $E_a = 8,000 J/mole$, which is a value representative of CH_4-air combustion. The DVODE algorithm of Byrne and Dean (1993) is employed to perform the numerical integration of the chemical reaction rate.

The initial and boundary conditions for the mean value of the progress variable at $x_1^* = 0$, are set with the following hyperbolic profile,

$$\widetilde{c}(x_3) = \frac{c_q + c_p}{2} + \frac{c_q - c_p}{2} \tanh\left(\frac{2h(x_3)}{\delta_m} - \frac{2h_p}{\delta_m}\right), \tag{15}$$

where, c_q and c_p are the mean values of the progress variable of the auxiliary burner ($c_q = 1$; $T_b = 2000$ K) and of the main duct ($c_p = 0$; $T_u = 560$ K), respectively. The quantity h_p is the height of auxiliary duct. Concerning the Monte Carlo simulation, 50 particles per control volume are used and the Mil-

stein scheme is employed for the numerical integration of the system of SDEs.

Figure (21) shows instantaneous fields of the chemical reaction progress variable $\widetilde{c}$ and the filtered chemical reaction rate $\widetilde{S}(c)$ for the present set of numerical simulations. The method of turbulent inflow data generation clearly influences the shear layer spreading rate as well as the position of the instantaneous filtered flame front. For instance, if we consider the subfigure (a) of Fig. 21, the longitudinal span of the turbulent flame front obtained with the white noise is larger than the one obtained using the other three methods.

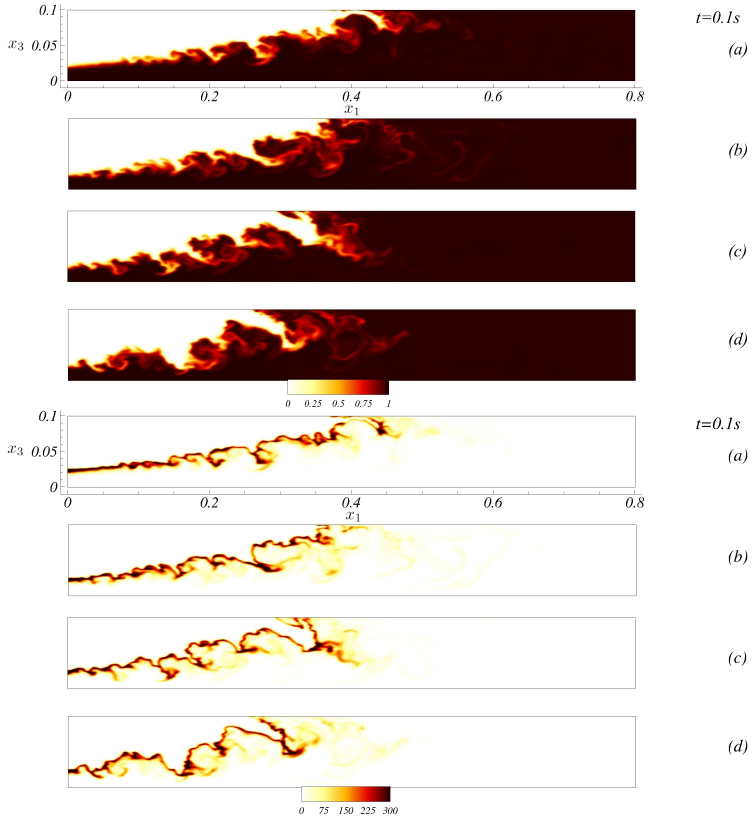

Figure 21: Instantaneous fields of chemical reaction progress variable $\widetilde{c}$ - top, and chemical reaction rate $\widetilde{S}(c)$ - bottom. The subfigures (a), (b), (c), and (d) display results of simulations with the respective inlet boundary condition methods: WN, DF, RFG and SEM.

Concerning the influence of the inlet boundary condition, we observe in Fig. 22 that accounting for a turbulence spectrum always gives rise to a shorter and thicker flame brush. The length of the 2D flame brush, based on the location of the iso-line $\langle c \rangle = 0.9$ in the x_1 direction, is found to be 560 mm for the simulation carried out with the superimposition of a white noise, while for the DF, RFG and SEM methods the lengths are 543, 497 and 414 mm respectively.

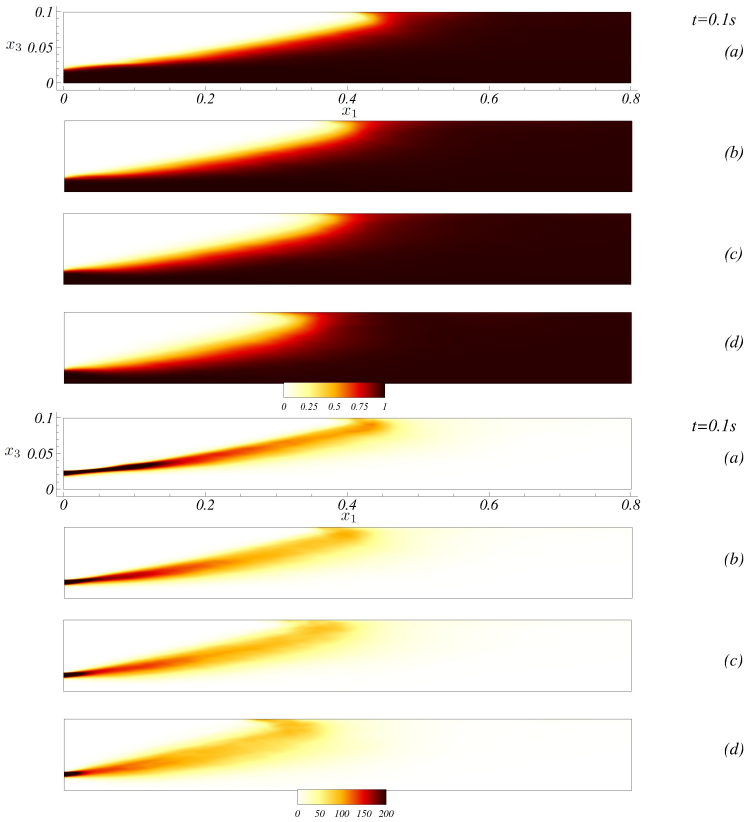

Figure 22: Averaged fields of the progress variable - top, and chemical reaction rate $S(c)$ - bottom. The subfigures (a), (b), (c), and (d) are results of simulations with the respective inlet boundary condition methods: WN, DF, RFG and SEM.

Finally, an interesting point that can be evidenced from the present investigation is to determine how the choice of the method of generation of turbulent inflow data may affect the representation of the flame-turbulence interaction.

To this purpose, we recall the definition of the Damköhler number, $Da = \tau_t/\tau_c$, which is the ratio of the characteristic turbulent time scale, τ_t and the chemical time scale, τ_c. This number is one of the quantities that characterizes how turbulence interacts with chemical reactions. It should be noted that the different synthetic turbulence generators may lead to different Damköhler number values.

Indeed, the characteristic time of turbulence is strongly affected by the different methods retained to generate inflow data. Considering the white noise technique, we observed that the fluctuations lie in the range $1-20$ m/s, whereas using the DF, RFG and SEM methods, the maximum value of fluctuations downstream of the flame brush are about 60, 40 and 70 m/s respectively. Given the grid size and the computational domain retained in the present study, which provide a minimum length of the control volumes of 1 mm, the turbulent characteristic times for the WN, DF, RFG and SEM methods are $50\,\mu s$, $16\,\mu s$, $25\,\mu s$ and $14\,\mu s$, respectively. For the cases simulated in the present work, the Damköhler number value is found to be 0.11 for the white noise. For the simulations performed with the DF, RFG and SEM methods, the Damköhler number is 0.033, 0.055 and 0.03, respectively which clearly confirms how the results of turbulent reactive flow simulations may be sensitive to the methodology used to generate synthetic turbulence at inlet boundary conditions.

7.2. Three-dimensional versus two-dimensional numerical simulations

The reactive numerical simulations that are reported herein have been performed using the PDF closure presented in section 3.1. Large Eddy Simulations should theoretically be performed in 3D, but the present reactive computations, which do involve the resolution of the PDF transport equation with a Lagrangian Monte-Carlo solver, remain quite expensive. This is the reason why we have resorted to 2D simulations so as to evaluate the sensivity of the computational results to the four inlet turbulence generators. However, it is quite relevant to question the use and impact of the 2D approximation. This point is still under investigation but, for one given inlet turbulence generator, a preliminary answer is provided in this last section of the manuscript.

The computational domain is now a three-dimensional box with dimensions $(800\times50\times100)$ mm^3, discretized with a mesh of $320\times50\times100$ control volumes in the x_1, x_2 and x_3-direction, respectively. The computational domain is divided into 256 parallel regions, each featuring 6250 control volumes. No-slip boundary conditions are imposed over x_2 and x_3-direction while the Orlanski's advective boundary condition is again used at the outlet. The RFG model is retained to generate the turbulent inflow data.

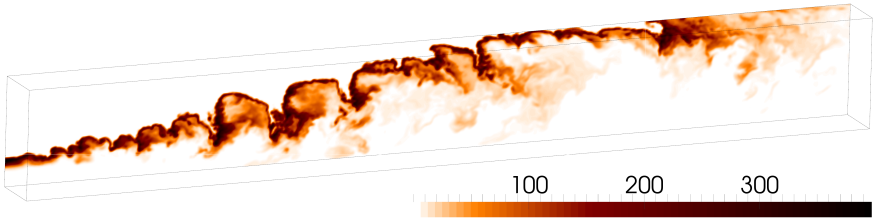

Figure 23: Instantaneous fields of the filtered chemical reaction rate $\widetilde{S}(c)$ in s^{-1}.

Figures 23 and 24 display the instantaneous fields of the filtered chemical reaction rate and filtered progress variable. Figure 25 illustrates the important flow acceleration that is induced by the thermal heat release. Combustion is initiated just downstream of the channel entrance and further develops along the channel length to reach an anchoring position at the upper channel wall at around $x_1 = 400$ mm downstream of the splitter plate, which is consistent with the data gathered from experimental investigations.The flame is subject to a large turbulence intensity and, as a consequence, the filtered flame structure appears to be strongly wrinkled by the large-scale turbulence. From a qualitative point of view, the filtered flame features a thickness of the order of centimeters. A similar order of magnitude was reported from the experimental observations of Magre et al. Magre et al. (1988). Nevertheless, it is important to emphasize that the LES results cannot be used to provide a statement about possible flamelet broadening. LES provides only space-filtered quantities, in such a manner that a direct comparison between numerical and experimental results can be performed

in a time-averaged statistical sense only. Such a comparison is reported in Fig. 26.

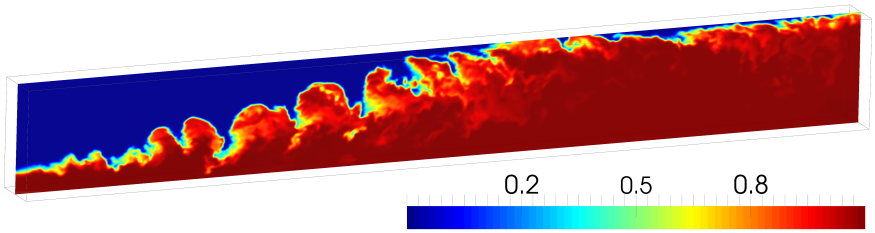

Figure 24: Instantaneous fields of the filtered progress variable $\widetilde{c}$ (bottom).

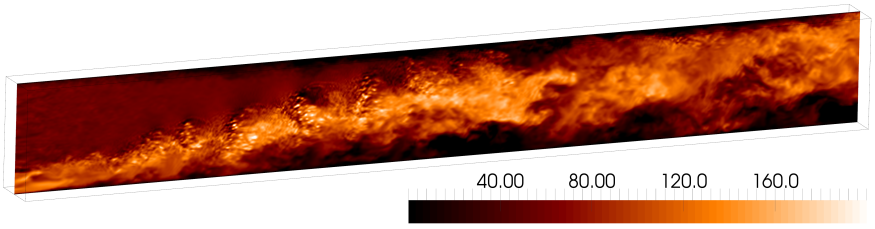

Figure 25: Instantaneous field of the $\widetilde{u}_1$ filtered velocity component.

Comparing the temperature profiles obtained numerically with the experiment, it is possible to observe in Fig. 26 that a reasonable level of agreement is achieved. From the comparison between 2D and 3D results with experiments, it seems that the 2D approximation offers a rather satisfactory picture of the average temperature field. At the very least, the 3D computational results does not cast doubt on the representativeness of the 2D results. Finally, it should be acknowledged that the limitations associated to the modeling of the chemical kinetics, i.e., global single-step chemistry, as well as the uncertainties that remain in the closure of micro-mixing terms for premixed conditions (Mura et al., 2003; Mura and Champion, 2009), suffice to explain the residual differences observed between computational results and experimental data.

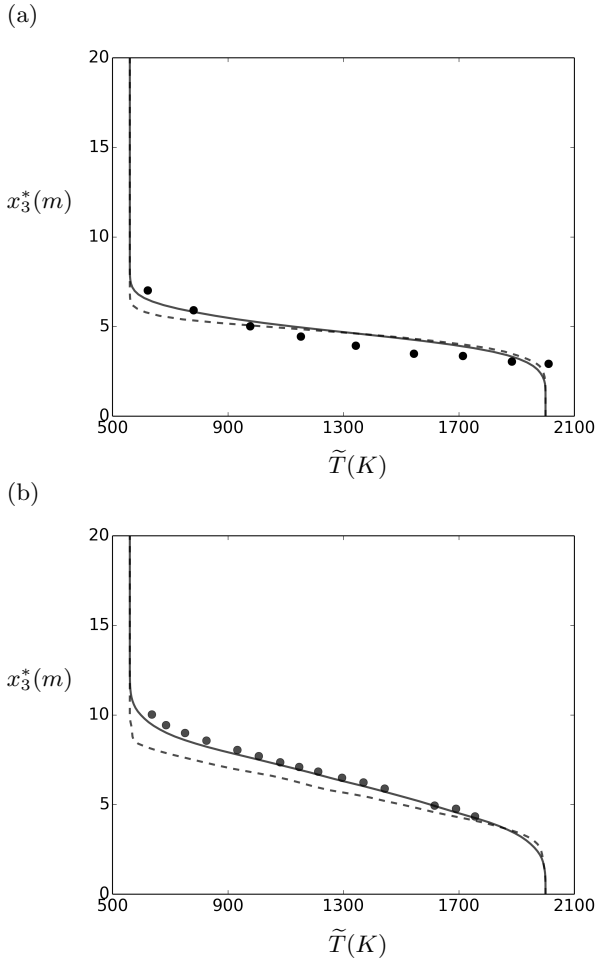

Figure 26: Mean temperature profile at (a): $x_1^* = 8.4$ (top) and (b): $x_1^* = 24.4$ (bottom); • Experimental data; (—) 2D results; (- -) 3D results.

8. Conclusion

Large Eddy Simulations of both reactive and non-reactive turbulent channel flows of methane/air mixtures have been conducted with special emphasis placed on the influence of turbulent inlet Boundary Conditions. The analysis undoubtedly confirms the sensitivity of the obtained results to the choice of the synthetic turbulence generator retained at the inlet of the computational domain. For the sake of completeness this sensitivity study is conducted for four

distinct turbulent inflow conditions including *white noise* (WN), *digital filter* (DF) by Klein et al. (2003), *random flow generator* (RFG) by Smirnov et al. (2001), and *synthetic eddy model* (SEM) of Jarrin et al. (2009). The capability of each method to reproduce a prescribed Reynolds stress tensor at the inlet BC is first evaluated quantitatively. The energy spectrum associated with the corresponding fluctuating velocity field are also examined. This analysis provides some interesting bases to explain the behavior that is observed when the synthetic turbulence generators are used to perform three-dimensional LES of high-speed mixing layers. The computational results of the corresponding LES are investigated in details and the quality of the agreement with experimental data is found to be significantly improved by resorting to elaborated synthetic turbulence generators that accounts for the large scale dynamics and coherence. The results obtained for reactive flow conditions also clearly emphasize the influence of the retained model on the chemical rate statistics, which confirms the importance of this issue for the LES of turbulent reactive flows. From the computational cost point of view, the DF, RFG and SEM methods obviously require longer CPU time than the WN. For the present applications, the additional CPU costs lie between 35 per cent for the method of Smirnov et al. (2001), and 55 per cent for the method of Klein et al. (2003), which remains moderate considering the potential improvements that may be obtained from their use. Finally, in the light of the obtained results, the RFG and SEM frameworks are found to offer the best compromises between computational costs and physical relevance.

Acknowledgments

These results have been obtained as a part of the PhD thesis of J.M. Vedovoto and have been presented at the Eighth International Symposium on Turbulence and Shear Flow Phenomena (TSFP-8) held in August 2013 in Poitiers (France). The research of A. Mura benefited from the HPC resources GENCI-IDRIS (Grant 2013-x20132a0912). The authors would like to thank CNPq, FAPEMIG and PETROBRAS S.A. for the financial support.

References

Albin, E., D'Angelo, Y., Vervisch, L., 2011. Flow streamline based navier-stokes characteristic boundary conditions: modeling for transverse and corner outflows. Computers and Fluids 51, 115–126.

Andrade, F.O., Figueira da Silva, L.F., Mura, A., 2011. Large eddy simulation of turbulent premixed combustion at moderate damköhler numbers stabilized in a high speed flow. Combustion Science and Technology 183, 645–664.

Bardina, J., Ferziger, J.H., Reynolds, W.C., 1980. Improved subgrid models for large eddy simulation. AIAA Paper 1357.

Batten, P., Goldberg, U., Chakravarthy, S., 2004. Interfacing statistical turbulence closures with large-eddy simulation. AIAA Journal 42, 485–492.

Bilger, R., Pope, S., Bray, K., Driscoll, J., 2005. Paradigms in turbulent combustion research. Proceedings of the Combustion Institute 30, 21–42.

Bodony, D., 2006. Analysis of sponge zones for computational fluid mechanics. Journal of Computational Physics 212, 681–702.

Brucker, K.A., Sarkar, S., 2007. Evolution of an initially turbulent stratified shear layer. Physics of Fluids 19, 105105.

Byrne, G.D., Dean, A.M., 1993. The numerical solution of some kinetics models with vode and chemkin ii. Computers & Chemistry 17, 297 – 302.

Colucci, P.J., Jaberi, F.A., Givi, P., Pope, S.B., 1998. Filtered density function for large eddy simulation of turbulent reacting flows. Physics of Fluids 10, 499.

Davidson, L., Billson, M., 2004. Hybrid les-rans using synthetized turbulence for forcing at the interface, in: ECCOMAS (Ed.), Proccedings of the 4th European Congress on Computational Methods in Applied Sciences and Engineering - ECCOMAS 2004, Jyväskylä, Finland.

Dopazo, C., O'Brien, E.E., 1974. An approach to the autoignition of a turbulent mixture. Acta Astronautica 1, 1239–1266.

Druault, P., Lardeau, S., Bonnet, J.P., Coiffet, F., Delville, J., Lamballais, E., Largeau, J.F., Perret, L., 2004. Generation of three-dimensional turbulent inlet conditions for large-eddy simulation. AIAA Journal 42, 447–456.

Ferziger, J., Peric, M., 1996. Computational methods for fluid dynamics. Springer.

Fox, R.O., 2003. Computational models for turbulent reacting flows. Cambridge University Press.

Fureby, C., 2008. Towards the use of Large Eddy Simulation in engineering. Progress in Aerospace Science 54, 381–396.

Gardiner, C., 2009. Stochastic methods: a handbook for the natural and social sciences. Springer.

Germano, M., 1992. Turbulence: the filtering approach. Journal of Fluid Mechanics 238, 325–336.

Haworth, D., 2010. Progress in probability density function methods for turbulent reacting flows. Progress in Energy and Combustion Science 36, 168–259.

Jarrin, N., Prosser, R., Uribe, J.C., Benhamadouche, S., Laurence, D., 2009. Reconstruction of turbulent fluctuations for hybrid RANS/LES simulations using a Synthetic-Eddy Method. International Journal of Heat and Fluid Flow 30, 435–442.

Keating, A., Piomelli, U., Balaras, E., Kaltenbach, H., 2004. A priori and a posteriori tests of inflow conditions for large eddy simulation. Physics of Fluids 16, 4696–4712.

Klein, M., Sadiki, A., Janicka, J., 2003. A digital filter based generation of inflow data for spatially developing direct numerical or large eddy simulations. Journal of Compututational Physics 186, 652–665.

Kloeden, P.E., Platen, E., 2000. Numerical Solution of Stochastic Differential Equations (Stochastic Modelling and Applied Probability). Springer.

Kraichnan, R.H., 1970. Diffusion by a random velocity field. Physics of Fluids 13, 22–31.

Le, H., Moin, P., Kim, J., 1997. Direct numerical simulation of turbulent flow over a backward-facing step. Journal of Fluid Mechanics 330, 349–374.

Lee, S., Lele, S.K., Moin, P., 1992. Simulation of spatially evolving turbulence and the applicability of taylor's hypothesis in compressible flow. Physics of Fluids A Fluid Dynamics 4, 1521–1530.

Li, N., Balaras, E., Piomelli, U., 2000. Inflow conditions for large-eddy simulations of mixing layers. Physics of Fluids 12, 935–938.

Lilly, D., 1992. A proposed modification of the Germano subgrid-scale closure method. Physics of Fluids A: Fluid Dynamics 4, 633.

Liu, S., Meneveau, C., Katz, J., 1994. On the properties of similarity subgrid-scale models as deduced from measurements in a turbulent jet. Journal of Fluid Mechanics 275, 83–120.

Lumley, J.L., 1967. The structure of inhomogeneous turbulence, in: Yaglom, A.M., Tatarski, V.I. (Eds.), Atmospheric turbulence and wave propagation. Nauka, Moscow, pp. 166–178.

Lund, T., 1998. Generation of turbulent inflow data for spatially-developing boundary layer simulations. Journal of Computational Physics 140, 233–258.

Magre, P., Moreau, P., Collin, G., Borghi, R., Péalat, M., 1988. Further studies by cars of premixed turbulent combustion in a high velocity flow. Combustion and Flame 71, 147 – 168.

Moreau, P., Boutier, A., 1977. Laser velocimeter measurements in a turbulent flame. Symposium (International) on Combustion 16, 1747 – 1756.

Mura, A., Champion, M., 2009. Relevance of the bray number in the small-scale modeling of turbulent premixed flames. Combustion and Flame 156, 729 – 733.

Mura, A., Galzin, F., Borghi, R., 2003. A unified pdf-flamelet model for turbulent premixed combustion. Combustion Science and Technology 175, 1573–1609.

Orlanski, I., 1976. A simple boundary condition for unbounded hyperbolic flows. Journal of Computational Physics 21, 251 – 269.

Poinsot, T.J., Lele, S.K., 1992. Boundary conditions for direct simulations of compressible viscous flows. Journal of Computational Physics 101, 104 – 129.

Pope, S.B., 1985. Pdf methods for turbulent reactive flows. Progress in Energy and Combustion Science 11, 119–192.

Raman, V., 2004. Hybrid finite-volume/transported PDF simulations of a partially premixed methane-air flame. Combustion and Flame 136, 327–350.

Rogallo, R.S., 1981. Numerical experiments in homogeneous turbulence. Nasa Technical Memorandum 81.

Rudy, D., Strikwerda, J., 1980. A nonreflecting outflow boundary condition for subsonic navier-stokes calculations. Journal of Computational Physics 36, 55–70.

Sagaut, P., Deck, S., Terracol, M., 2006. Multiscale and multiresolution approaches in turbulence. Imperial Colllege Press.

Schlüter, J., Moin, P., Pitsch, H., 2004. Large-Eddy Simulation inflow conditions for coupling with Reynolds-averaged flow solvers. AIAA Journal 42, 478–484.

Schneider, G.E., Zedan, M., 1981. A modified strongly implicit procedure for the numerical solution of field problems. Numerical Heat Transfer 4, 1–19.

Smirnov, A., 2004. Random flow generation procedure technical manual , 1–13.

Smirnov, A., Shi, S., Celik, I., 2001. Random flow generation technique for large eddy simulations and particle-dynamics modeling. Journal of Fluids Engineering 123, 359–371.

Tabor, G., Baba-Ahmadi, M., 2010. Inlet conditions for large eddy simulation: A review. Computers & Fluids 39, 553–567.

Thompson, K., 1987. Time-dependent boundary conditions for hyperbolic systems. Journal of Computational Physics 68, 1–24.

Vedovoto, J.M., da Silveira Neto, A., Mura, A., Figueira da Silva, L.F., 2011. Application of the method of manufactured solutions to the verification of a pressure-based finite-volume numerical scheme. Computers & Fluids 51, 85 – 99.

Villermaux, J., Devillon, J.C., 1972. Representation de la coalescence et de la redispersion des domaines de segregation dans un fluide par un modele d'interaction phenomenologique. Second International Symposium on Chemical Reaction Engineering , 1–13.

Williams, F.A., 1985. Combustion theory. volume 54. The Benjamin/Cummings Publishing Company, Inc., 2nd ed.

Zhang, Y.Z., Haworth, D.C., 2004. A general mass consistency algorithm for hybrid particle/finite-volume pdf methods. Journal of Computational Physics 194, 156 – 193.